

# FLUCTUATION EXCHANGE ANALYSIS OF SUPERCONDUCTIVITY IN THE STANDARD THREE-BAND $\text{CuO}_2$ MODEL

Gökhan Esirgen and N. E. Bickers

*Institute for Theoretical Physics*

*University of California*

*Santa Barbara, CA 93106-4030*

*and*

*Department of Physics and Astronomy*

*University of Southern California*

*Los Angeles, CA 90089-0484*

The fluctuation exchange, or FLEX, approximation for interacting electrons is applied to study instabilities in the standard three-band model for  $\text{CuO}_2$  layers in the high-temperature superconductors. Both intra-orbital and near-neighbor Coulomb interactions are retained. The filling dependence of the  $d_{x^2-y^2}$  transition temperature is studied in both the “hole-doped” and “electron-doped” regimes using parameters derived from constrained-occupancy density-functional theory for  $\text{La}_2\text{CuO}_4$ . The agreement with experiment on the overdoped hole side of the phase diagram is remarkably good, i.e., transitions emerge in the 40 K range with no free parameters. In addition the importance of the “orbital antiferromagnetic,” or flux phase, charge density channel is emphasized for an understanding of the underdoped regime.

71.10.+x, 71.20.Ad, 74.65.+n

## I. INTRODUCTION

An experimental consensus has developed in recent years that the order parameter in the high-temperature cuprate superconductors has  $d_{x^2-y^2}$  symmetry.<sup>1</sup> Well before experiments indicated this exotic symmetry a variety of theoretical approaches had suggested a tendency toward  $d_{x^2-y^2}$  pairing in the Hubbard<sup>2-4</sup> and  $t - J$  models.<sup>5</sup> Within weak-coupling approaches, which treat the Coulomb interaction as a perturbation to one-electron band theory, exchange of antiferromagnetic spin fluctuations<sup>6</sup> leads to pairing.

While the correctness of the spin fluctuation scenario remains controversial, it is of interest to examine the pairing process within a more realistic setting than the one-band Hubbard model. It is well-established that magnetism in the “undoped” cuprates can be understood within the context of a three-band model<sup>7</sup> (which projects to a  $t - J$  model<sup>8</sup> in the strong-coupling limit). This  $\text{CuO}_2$  model describes nearly filled Cu  $3d_{x^2-y^2}$ , O  $2p_x$ , and O  $2p_y$  orbitals, which form a two-dimensional square Bravais lattice with a three-atom unit cell. The largest Coulomb integrals<sup>9-11</sup> in the  $\text{CuO}_2$  model are the repulsion between holes on the same d orbital ( $U_{dd} \sim 10$  eV) or p orbital ( $U_{pp} \sim 4$  eV), and the repulsion between holes on neighboring d and p orbitals ( $U_{pd} \sim 1$  eV).

A self-consistent and conserving calculation of one-particle properties in the  $\text{CuO}_2$  model based on exchange of magnetic and charge density fluctuations has been carried out previously.<sup>12,13</sup> In the present paper we extend this fluctuation exchange, or “FLEX,” calculation to an analysis of eigenvalues of the particle-particle and particle-hole vertex functions and the resulting transition temperatures. In particular, this analysis is carried out using one- and two-particle matrix elements deduced from constrained-occupancy density functional theory,<sup>9</sup> with no additional model projections or parameter fits. The results of this calculation with no adjustable parameters are, if not compelling, at least suggestive.

While the FLEX approach is inherently approximate, the observed trends in eigenvalues and transition temperatures for variations in hole density and Coulomb integrals can be expected to be carried over in more exact treatments. In addition this calculation provides a detailed example of the melding of many-body and band theory techniques now possible.

The paper is organized as follows: The model and calculational notation are summarized in Section II. The particle-particle and particle-hole vertex functions within the FLEX approximation are derived in a computationally tractable form in Section III. After a brief digression on sources of error, results for eigenvalues, transition temperatures, and eigenfunctions are presented in Section IV. The implications of the calculation are discussed, along with an overall summary, in Section V.

## II. MODEL AND NOTATION

In this section we define our notational conventions for the model to be studied. The three-orbital model for superconducting cuprate layers may be written in terms of creation operators for holes or electrons. As in Reference 12, which we hereafter denote “EB,” we adopt the hole representation; as an example,  $c_{d\sigma}^\dagger(\mathbf{R})$  creates a  $3d_{x^2-y^2}$  hole with spin  $\sigma$  in unit cell  $\mathbf{R}$ . In addition we choose a staggered orbital phase which helps simplify the analysis of two-particle eigenstates. The unit cell and phase conventions are illustrated in Figure 1. The Hamiltonian is conveniently broken

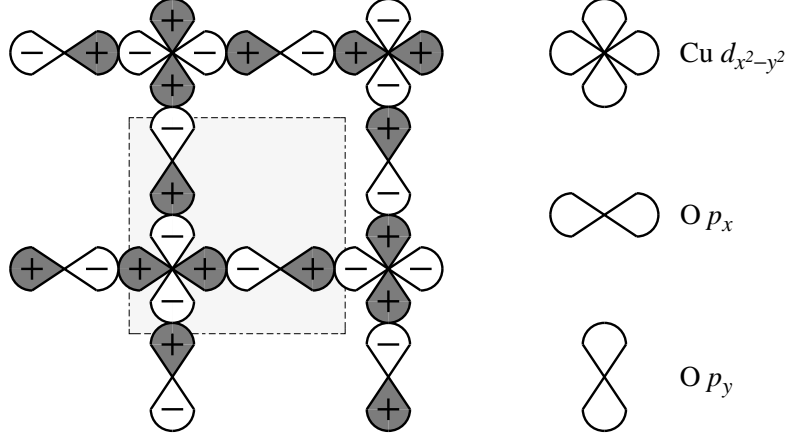


FIG. 1. Unit cell and orbital phase conventions. The unit cell contains three orbitals: the Cu  $3d_{x^2-y^2}$ , the O  $2p_x$  on x-axis bonds, and the O  $2p_y$  on y-axis bonds. The orbital phases are chosen in a checkerboard pattern. This assures that near-neighbor Cu–O and O–O hopping integrals have the same sign in all unit cells and greatly simplifies the two-body eigenstate analysis.

up into one-particle and two-particle components

$$\hat{H} = \hat{H}_0 + \hat{V} . \quad (1)$$

With our conventions the one-particle Hamiltonian takes the form

$$\begin{aligned} \hat{H}_0 - \mu N = & (\varepsilon_d - \mu) \sum_{\mathbf{R}} n_d(\mathbf{R}) + (\varepsilon_d - \mu + \varepsilon) \sum_{\mathbf{R}} [n_x(\mathbf{R}) + n_y(\mathbf{R})] \\ & - t_{pd} \sum_{\sigma, \mathbf{R}} \left[ c_{d\sigma}^\dagger(\mathbf{R}) c_{x\sigma}(\mathbf{R}) + c_{d\sigma}^\dagger(\mathbf{R} + \hat{x}) c_{x\sigma}(\mathbf{R}) \right. \\ & \left. + c_{d\sigma}^\dagger(\mathbf{R}) c_{y\sigma}(\mathbf{R}) + c_{d\sigma}^\dagger(\mathbf{R} + \hat{y}) c_{y\sigma}(\mathbf{R}) + H.C. \right] \\ & - t_{pp} \sum_{\sigma, \mathbf{R}} \left[ c_{y\sigma}^\dagger(\mathbf{R}) c_{x\sigma}(\mathbf{R}) + c_{y\sigma}^\dagger(\mathbf{R} + \hat{x}) c_{x\sigma}(\mathbf{R}) \right. \\ & \left. + c_{y\sigma}^\dagger(\mathbf{R} - \hat{y}) c_{x\sigma}(\mathbf{R}) + c_{y\sigma}^\dagger(\mathbf{R} + \hat{x} - \hat{y}) c_{x\sigma}(\mathbf{R}) + H.C. \right] . \end{aligned} \quad (2)$$

The number operators  $n_d$ ,  $n_x$  and  $n_y$  are defined in the usual way, e.g.,

$$n_d(\mathbf{R}) = \sum_{\sigma} c_{d\sigma}^\dagger(\mathbf{R}) c_{d\sigma}(\mathbf{R}) . \quad (3)$$

The physical values of the short-range hopping matrix elements  $t_{pd}$  and  $t_{pp}$  are both positive.<sup>9,10</sup> The d-hole creation energy  $\varepsilon_d$  may be set to zero without loss, and the p–d energy level difference  $\varepsilon$  is positive.

In the two-body Hamiltonian  $\hat{V}$  we retain the three largest Coulomb integrals from constrained-occupancy density functional studies:<sup>9,10</sup> The on-site Cu repulsion  $U_{dd}$ , the on-site O repulsion  $U_{pp}$ , and the near-neighbor Cu–O repulsion  $U_{pd}$ . The last interaction complicates the analysis since it has both intra-cell and inter-cell components. The Coulomb

interactions may be written in a spin-diagonalized form which allows a decoupling of  $S = 0$  (density) and  $S = 1$  (magnetic) excitations. This procedure is treated at length in EB.

The one-particle propagators for the Hamiltonian described above take the form

$$G_{ab}(\mathbf{R}_a, \tau_a; \mathbf{R}_b, \tau_b) = G_{ab}(\Delta\mathbf{R}_{ab}, \Delta\tau_{ab}) \equiv -\langle T_\tau c_a(\mathbf{R}_a, \tau_a) c_b^\dagger(\mathbf{R}_b, \tau_b) \rangle, \quad (4)$$

where  $(a, \mathbf{R}_a, \tau_a)$  and  $(b, \mathbf{R}_b, \tau_b)$  are the orbital, unit-cell, and imaginary-time labels for particles in the final and initial states (see Figure 2). Reference 12 describes the general procedure for calculating such propagators and provides



FIG. 2. Diagrammatic representation of the one-particle propagator  $G_{ab}(\Delta\mathbf{R}_{ab}, \Delta\tau_{ab})$ .

detailed results for the CuO<sub>2</sub> model described above. For the remainder of this paper we make use of one-particle properties obtained in this previous study.

### III. DERIVATION OF VERTEX FUNCTIONS

The calculation of eigenvalues of the particle-particle kernel in the CuO<sub>2</sub> model is conceptually straightforward, but notationally involved. It is assumed that self-consistent one-particle propagators  $G$  have been obtained using the technique described in EB. Functional differentiation of the off-diagonal self-energy in the presence of an external pairing field yields the irreducible particle-particle vertex  $\Gamma^{\text{PP}}$ . Using the notation developed in Reference 14 the singlet and triplet parts of the vertex are as follows (see Figure 3):

$$\begin{aligned} \Gamma_s^{\text{PP}}(12; 34) &= V_s(12; 34) \\ &+ \frac{1}{2}\Phi_d(24; 31) - \frac{3}{2}\Phi_m(24; 31) + \frac{1}{2}\Phi_d(14; 32) - \frac{3}{2}\Phi_m(14; 32), \end{aligned} \quad (5)$$

$$\begin{aligned} \Gamma_t^{\text{PP}}(12; 34) &= V_t(12; 34) \\ &+ \frac{1}{2}\Phi_d(24; 31) + \frac{1}{2}\Phi_m(24; 31) - \frac{1}{2}\Phi_d(14; 32) - \frac{1}{2}\Phi_m(14; 32). \end{aligned} \quad (6)$$

The numerical indices represent the space and time degrees of freedom of each particle, i.e.,

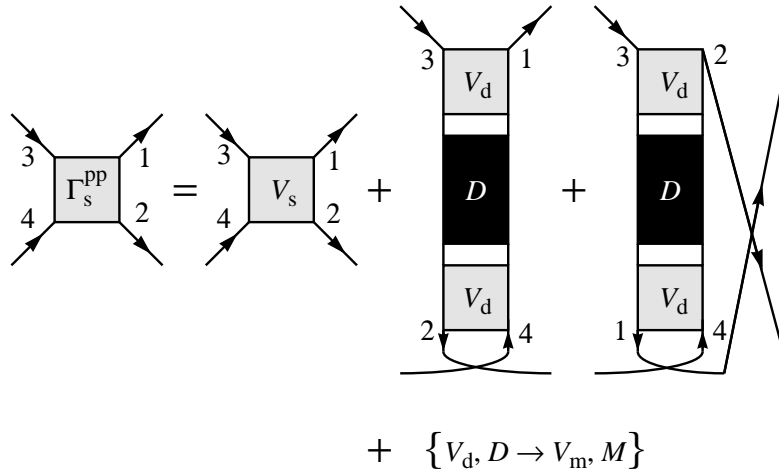


FIG. 3. Irreducible singlet vertex function  $\Gamma_s^{\text{PP}}$  within the FLEX approximation. Outgoing states are represented on the right of the diagrams, incoming states on the left. (The coefficients  $1/2$  and  $-3/2$  are omitted for clarity; see Equation (5).)  $V_s$  is the unrenormalized Coulomb matrix element in the singlet channel. The vertical ladders represent the exchange of density fluctuations.

$$1 \equiv (m_1, \mathbf{R}_1, \tau_1), \quad (7)$$

with  $m_1$  the orbital,  $\mathbf{R}_1$  the unit-cell displacement, and  $\tau_1$  the imaginary time coordinate for particle 1.

The matrix functions  $\Phi_d$  and  $\Phi_m$  represent particle-hole ladders in the density and magnetic channels:

$$\Phi_r(12; 34) = [V_r G^{\text{ph}}(\mathbf{1} - V_r G^{\text{ph}})^{-1} V_r](12; 34) \quad (8)$$

for  $r = d$  and  $m$ . The matrices  $V_r$  are the spin-diagonalized Coulomb interactions in each channel, and the matrix  $G^{\text{ph}}$  is the uncorrelated particle-hole propagator:

$$\begin{aligned} G^{\text{ph}}(12; 34) &= \beta \langle T_\tau c(1) c^\dagger(3) \rangle \langle T_\tau c(4) c^\dagger(2) \rangle \\ &= \beta G(13) G(42), \end{aligned} \quad (9)$$

with  $\beta$  the inverse temperature.

As usual,<sup>12</sup> matrix multiplication is defined by

$$(AB)(12; 34) = A(12; 56) B(56; 34), \quad (10)$$

with an implied sum on repeated indices. The singlet and triplet kernels are obtained by multiplying the vertex functions by the uncorrelated particle-particle propagator

$$G^{\text{pp}}(12; 34) = -\frac{1}{2}\beta G(13) G(24). \quad (11)$$

Note the presence of  $\frac{1}{2}$  in this definition of the propagator, which is consistent with our normalization of the vertex functions below.

Expressions for the density and magnetic Coulomb matrix elements  $V_d$  and  $V_m$  have been given previously in EB. Explicit expressions for  $V_s$  and  $V_t$  follow from the diagrams in Figure 4. As in our previous work, it is convenient

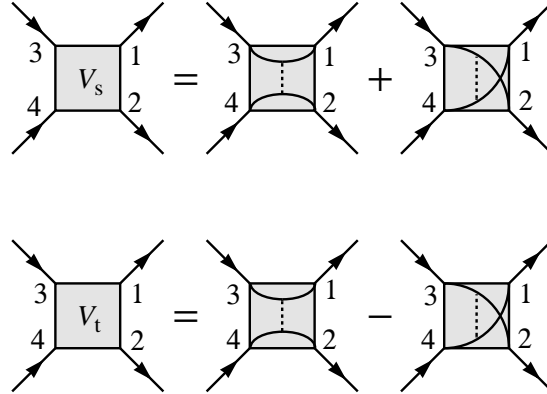


FIG. 4. Representation of the unrenormalized singlet and triplet Coulomb matrix elements  $V_s$  and  $V_t$ .

to adopt a notation which emphasizes the dependence of the matrix elements on only three unit-cell displacements between the two initial-state and two final-state particles (see Figure 5). Thus,  $V_s(\Delta\mathbf{R}_{ac}; ab, \Delta\mathbf{R}_{ab}; cd, \Delta\mathbf{R}_{cd})$  is the singlet Coulomb matrix element for a final-state particle pair in orbitals  $a$  and  $b$  with relative unit-cell displacement

$$\Delta\mathbf{R}_{ab} = \mathbf{R}_a - \mathbf{R}_b, \quad (12)$$

and an initial-state particle pair in orbitals  $c$  and  $d$  with relative unit-cell displacement  $\Delta\mathbf{R}_{cd}$ . The displacement between the initial and final state particles is given by  $\Delta\mathbf{R}_{ac}$ . There are only 11 two-particle states  $(ab, \Delta\mathbf{R}_{ab})$  which have non-zero singlet and triplet Coulomb matrix elements in the  $\text{CuO}_2$  model considered here. These states are listed in Table I for the unit-cell depicted in Figure 1. (An identically labeled 11-state basis for non-zero density and magnetic Coulomb matrix elements was defined in EB.)

As in EB, the initial/final state displacement  $\Delta\mathbf{R}_{ac}$  is conveniently eliminated in favor of a center-of-mass momentum  $\mathbf{Q}$  by writing

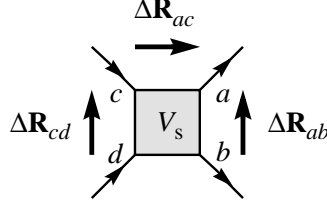


FIG. 5. Definition of unit-cell displacements in the representation of the singlet Coulomb matrix element.

Index	$a$	$b$	$\Delta \mathbf{R}_{ab}$
1	d	d	0
2	$p_x$	$p_x$	0
3	$p_y$	$p_y$	0
4	d	$p_x$	0
5	d	$p_x$	$+\hat{x}$
6	$p_x$	d	0
7	$p_x$	d	$-\hat{x}$
8	d	$p_y$	0
9	d	$p_y$	$+\hat{y}$
10	$p_y$	d	0
11	$p_y$	d	$-\hat{y}$

TABLE I. Indexing scheme for the minimum-range particle-particle basis set in the  $\text{CuO}_2$  model. The particle orbitals are  $a$  and  $b$ , with corresponding unit-cell displacement  $\Delta \mathbf{R}_{ab} \equiv \mathbf{R}_a - \mathbf{R}_b$ . Note that kernel eigenstates must satisfy the symmetry requirements of the Pauli Principle, but the basis states need not.

$$V_s(\mathbf{Q}; ab, \Delta \mathbf{R}_{ab}; cd, \Delta \mathbf{R}_{cd}) \equiv \sum_{\Delta \mathbf{R}_{ac}} e^{-i\mathbf{Q} \cdot \Delta \mathbf{R}_{ac}} V_s(\Delta \mathbf{R}_{ac}; ab, \Delta \mathbf{R}_{ab}; cd, \Delta \mathbf{R}_{cd}) . \quad (13)$$

The indices in Table I can then be used to write  $V_s$  and  $V_t$  compactly as  $\mathbf{Q}$ -dependent  $11 \times 11$  matrices. For example,

$$\begin{aligned} V_s^{33}(\mathbf{Q}) &= 2U_{pp} \\ V_s^{64}(\mathbf{Q}) &= -V_t^{64}(\mathbf{Q}) = U_{pd} \\ V_s^{75}(\mathbf{Q}) &= -V_t^{75}(\mathbf{Q}) = e^{iQ_x} U_{pd} . \end{aligned} \quad (14)$$

Though the basic Coulomb interactions  $V_s$  and  $V_t$  are short-ranged, the fluctuation-induced contributions to the particle-particle vertex functions  $\Gamma_s^{\text{pp}}$  and  $\Gamma_t^{\text{pp}}$  are not. Nevertheless, it is possible to calculate accurate pairing eigenvalues using vertex functions truncated in the relative displacement of the particle pair. For this reason it is convenient to arrive at a particle-particle vertex labeled using (i) total momentum-frequency  $Q \equiv (\mathbf{Q}, i\Omega)$ ; (ii) pair orbital indices  $(ab)$  ( $3 \times 3 = 9$  possible combinations for the three-orbital model); (iii) unit-cell displacement  $\Delta \mathbf{R}_{ab}$  of the pair elements; and (iv) relative frequency  $i\omega$ .<sup>15</sup> (There is no additional benefit in introducing a relative time coordinate, since the fluctuations induce long-range couplings in imaginary time.) Previous notation for the time-independent Coulomb matrix elements may be generalized in a natural way. The desired singlet and triplet vertex functions (see Figure 6(a)) take the form

$$\Gamma_r^{\text{pp}}(Q; m_1 m_2, \Delta \mathbf{R}_{12}, i\omega; m_3 m_4, \Delta \mathbf{R}_{34}, i\omega') . \quad (15)$$

In order to calculate the crossed-channel particle-hole ladders  $\Phi_d$  and  $\Phi_m$ , it is essential to use a different basis set obtained by a series of Fourier transforms. An initial Fourier transform on the relative displacement coordinates in Equation (5) yields

$$\begin{aligned} \Gamma_s^{\text{pp}}(Q; m_1 m_2, \Delta \mathbf{R}_{12}, i\omega; m_3 m_4, \Delta \mathbf{R}_{34}, i\omega') = \\ V_s(\mathbf{Q}; m_1 m_2, \Delta \mathbf{R}_{12}; m_3 m_4, \Delta \mathbf{R}_{34}) \end{aligned}$$

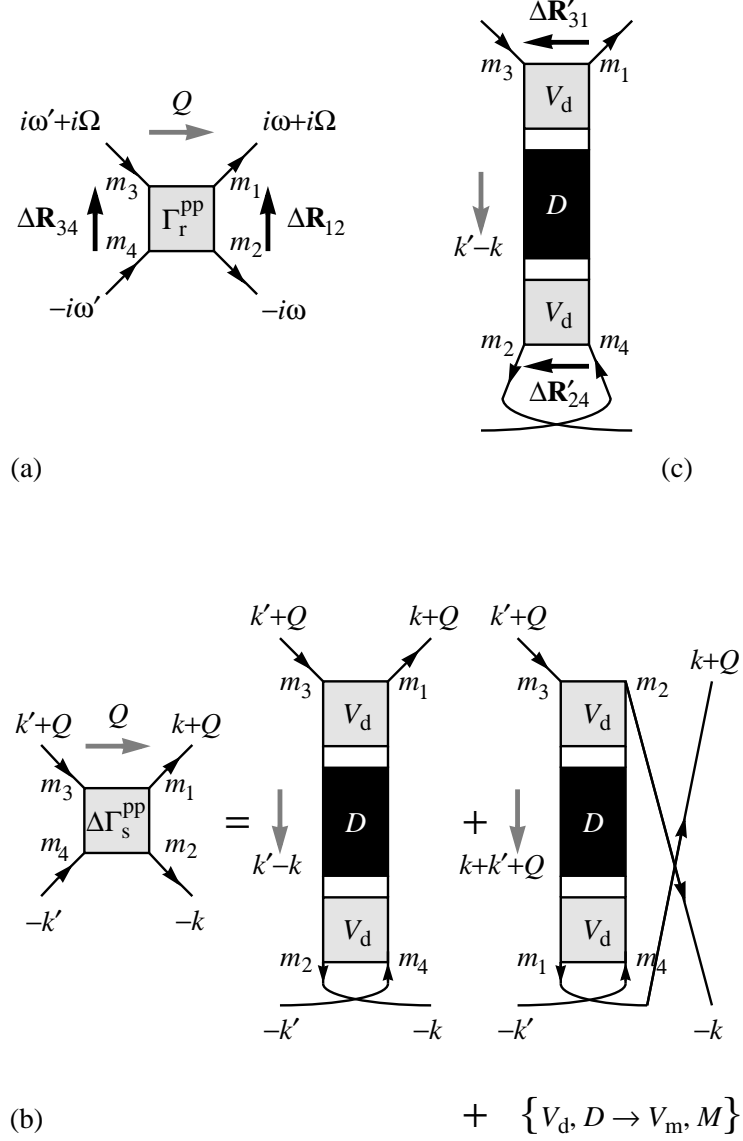


FIG. 6. Calculation of the irreducible particle-particle vertex functions  $\Gamma_r^{\text{pp}}$ ,  $r = s$  and  $t$ . (a) Diagrammatic representation of the irreducible vertex in the computationally optimal basis set. Note that the total center-of-mass momentum-frequency  $Q = (\mathbf{Q}, i\Omega)$  is conserved. (b) Fourier-transformed singlet vertex function  $\Delta\Gamma_s^{\text{pp}}(Q; m_1 m_2, k; m_3 m_4, k')$ . See also Equation (18). (c) Representation of the first particle-hole ladder in (b) in the relative displacement basis. See also Equation (19).

$$+ \frac{1}{N^2} \sum_{\mathbf{k}\mathbf{k}'} e^{i\mathbf{k}\cdot\Delta\mathbf{R}_{12}} \Delta\Gamma_s^{\text{PP}}(Q; m_1m_2, k; m_3m_4, k') e^{-i\mathbf{k}'\cdot\Delta\mathbf{R}_{34}} , \quad (16)$$

with

$$\begin{aligned} k &= (\mathbf{k}, i\omega) \\ k' &= (\mathbf{k}', i\omega') . \end{aligned} \quad (17)$$

The fluctuation-induced contribution  $\Delta\Gamma_s^{\text{PP}}$  takes the form

$$\begin{aligned} \Delta\Gamma_s^{\text{PP}}(Q; m_1m_2, k; m_3m_4, k') &= \\ \left[ \frac{1}{2}\Phi_d - \frac{3}{2}\Phi_m \right] (k' - k; m_2m_4, -k'; m_3m_1, k + Q) \\ + \left[ \frac{1}{2}\Phi_d - \frac{3}{2}\Phi_m \right] (k + k' + Q; m_1m_4, -k'; m_3m_2, -k) . \end{aligned} \quad (18)$$

The ladders are represented diagrammatically in Figure 6(b).

The first particle-hole ladder in Equation (18) may be translated back to the relative displacement basis (Figure 6(c)):

$$\begin{aligned} \Phi_d(k' - k; m_2m_4, -k'; m_3m_1, k + Q) &= \\ \sum_{\Delta\mathbf{R}'_{24}, \Delta\mathbf{R}'_{31}} e^{i\mathbf{k}'\cdot\Delta\mathbf{R}'_{24}} \Phi_d(k' - k; m_2m_4, \Delta\mathbf{R}'_{24}; m_3m_1, \Delta\mathbf{R}'_{31}) e^{i(\mathbf{k}+\mathbf{Q})\cdot\Delta\mathbf{R}'_{31}} . \end{aligned} \quad (19)$$

Note that primes are included on the displacements here to emphasize that they are dummy summation variables, at this stage unrelated to  $\Delta\mathbf{R}_{12}$  and  $\Delta\mathbf{R}_{34}$  in Equation (16). Similar expressions hold for the other ladder sum terms contributing to  $\Delta\Gamma_s^{\text{PP}}$ . Note that  $\Phi_d$  and  $\Phi_m$  are independent of the relative frequency variables (due to the instantaneous character of  $V_d$  and  $V_m$ ) and have been dropped from the notation without loss.

The expressions in Equations (16) and (19) each involve double Fourier transforms and are impractical to calculate numerically. A much simpler form for  $\Delta\Gamma$  may be derived by changing momentum variables and interchanging the order of sums. For example, for the first particle-hole ladder contribution the appropriate change of variables is

$$\begin{aligned} \mathbf{k}' - \mathbf{k} &\rightarrow \mathbf{Q}' \\ \mathbf{k}' &\rightarrow \mathbf{k}' . \end{aligned} \quad (20)$$

The sum on  $\mathbf{k}'$  may then be carried out explicitly, yielding a delta function, which collapses the sum on  $\Delta\mathbf{R}'_{24}$ .

After additional relabeling of summation variables, the complete result for  $\Gamma_s^{\text{PP}}$  which results from this procedure is

$$\begin{aligned} \Gamma_s^{\text{PP}}(Q; m_1m_2, \Delta\mathbf{R}_{12}, i\omega; m_3m_4, \Delta\mathbf{R}_{34}, i\omega') &= \\ V_s(\mathbf{Q}; m_1m_2, \Delta\mathbf{R}_{12}; m_3m_4, \Delta\mathbf{R}_{34}) \\ + \sum_{\Delta\mathbf{R}_{13}} e^{-i\mathbf{Q}\cdot\Delta\mathbf{R}_{13}} \Delta\Gamma_s^{\text{PP}}(\Delta\mathbf{R}_{13}, i\Omega; m_1m_2, \Delta\mathbf{R}_{12}, i\omega; m_3m_4, \Delta\mathbf{R}_{34}, i\omega') , \end{aligned} \quad (21)$$

with

$$\begin{aligned} \Delta\Gamma_s^{\text{PP}}(\Delta\mathbf{R}_{13}, i\Omega; m_1m_2, \Delta\mathbf{R}_{12}, i\omega; m_3m_4, \Delta\mathbf{R}_{34}, i\omega') &= \\ \frac{1}{N} \sum_{\mathbf{Q}'} e^{i\mathbf{Q}'\cdot\Delta\mathbf{R}_{23}} \left[ \frac{1}{2}\Phi_d - \frac{3}{2}\Phi_m \right] (\mathbf{Q}', i(\omega' - \omega); m_2m_4, \Delta\mathbf{R}_{24}; m_3m_1, \Delta\mathbf{R}_{31}) + \\ \frac{1}{N} \sum_{\mathbf{Q}'} e^{i\mathbf{Q}'\cdot\Delta\mathbf{R}_{13}} \left[ \frac{1}{2}\Phi_d - \frac{3}{2}\Phi_m \right] (\mathbf{Q}', i(\omega + \omega' + \Omega); m_1m_4, \Delta\mathbf{R}_{14}; m_3m_2, \Delta\mathbf{R}_{32}) , \end{aligned} \quad (22)$$

where all relative displacements are expressed in terms of  $\Delta\mathbf{R}_{13}$ ,  $\Delta\mathbf{R}_{12}$ , and  $\Delta\mathbf{R}_{34}$ :

$$\begin{aligned}
\Delta \mathbf{R}_{23} &= -\Delta \mathbf{R}_{32} = \Delta \mathbf{R}_{13} - \Delta \mathbf{R}_{12} \\
\Delta \mathbf{R}_{24} &= \Delta \mathbf{R}_{13} - \Delta \mathbf{R}_{12} + \Delta \mathbf{R}_{34} \\
\Delta \mathbf{R}_{31} &= -\Delta \mathbf{R}_{13} \\
\Delta \mathbf{R}_{14} &= \Delta \mathbf{R}_{13} + \Delta \mathbf{R}_{34} .
\end{aligned} \tag{23}$$

A similar expression for  $\Gamma_t^{\text{pp}}$  may be obtained immediately using the correspondence in Equation (6).

The ladder summations  $\Phi_d$  and  $\Phi_m$  may be calculated as matrix products in the space with compound indices  $(ab, \Delta \mathbf{R}_{ab})$ :

$$\Phi_r = -V_r \bar{\chi} (1 + V_r \bar{\chi})^{-1} V_r , \tag{24}$$

for  $r=d, m$ , where the uncorrelated fluctuation propagator  $\bar{\chi}$  is defined by

$$\bar{\chi}(Q; ab, \Delta \mathbf{R}_{ab}; cd, \Delta \mathbf{R}_{cd}) = -\frac{T}{N} \sum_{\mathbf{k}} e^{i\mathbf{k} \cdot (\Delta \mathbf{R}_{ab} - \Delta \mathbf{R}_{cd})} G_{ac}(k+Q) G_{db}(k) . \tag{25}$$

For the  $\text{CuO}_2$  model the required matrix inverse is only  $11 \times 11$ . Note, however, that a separate inverse must be calculated for each value of the particle-hole ladder's center-of-mass momentum-frequency.

The uncorrelated particle-particle propagator may also be expressed in the basis adopted above (Figure 7):

$$\begin{aligned}
G^{\text{pp}}(Q; m_1 m_2, \Delta \mathbf{R}_{12}, i\omega; m_3 m_4, \Delta \mathbf{R}_{34}, i\omega') = \\
-\frac{1}{2} \delta_{\omega\omega'} \frac{T}{N} \sum_{\mathbf{k}} e^{i\mathbf{k} \cdot (\Delta \mathbf{R}_{12} - \Delta \mathbf{R}_{34})} G_{m_1 m_3}(k+Q) G_{m_2 m_4}(-k) .
\end{aligned} \tag{26}$$

The particle-particle eigenvalue problem then takes the form

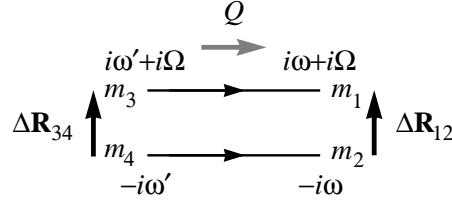


FIG. 7. Diagrammatic representation of the uncorrelated particle-particle propagator  $G^{\text{pp}}(Q; m_1 m_2, \Delta \mathbf{R}_{12}, i\omega; m_3 m_4, \Delta \mathbf{R}_{34}, i\omega')$ . Note the propagator is diagonal in the relative frequency, i.e., it vanishes for  $\omega \neq \omega'$ .

$$\Gamma_r^{\text{pp}}(Q) G^{\text{pp}}(Q) \phi(Q) = \lambda(Q) \phi(Q) , \tag{27}$$

for  $r = s$  and  $t$ . Note that with the conventions adopted here a positive eigenvalue indicates attraction. (Although the kernel is non-hermitian, it is possible to show for  $\Omega = 0$  that the particle-particle eigenvalues are real-valued or occur in complex conjugate pairs.) The matrices  $\Gamma_r^{\text{pp}}$  and  $G^{\text{pp}}$  operate in a far larger compound-index space than that defined previously for the Coulomb interactions  $V_r$ . The index now consists of the orbital-pair label  $(m_1 m_2)$ , which takes on nine values in the  $\text{CuO}_2$  problem; the subset of unit-cell displacements  $\Delta \mathbf{R}_{12}$  retained; and the set of values of the relative frequency  $\omega$  within a pre-defined cutoff interval.

Note that since the kernel matrix is non-hermitian, its sets of left and right eigenvectors are not simply related (even though the left and right eigenvalue spectra are identical.) In the following section we emphasize the real-space and frequency dependence of the right eigenvectors, i.e., those determined by Equation (27). This is natural since the right eigenvector at  $T_c$  evolves smoothly into the off-diagonal self-energy below  $T_c$ . (The right eigenvalue equation may be re-derived by linearizing a self-consistent field problem in the off-diagonal self-energy.) The corresponding left eigenvector has no such simple physical interpretation.

A number of powerful approaches have been developed in recent years to compute a few selected eigenvalues of a general non-hermitian matrix in cases such as this for which a full diagonalization is impractical. All such approaches are derived from the much more standard algorithms available for the real-symmetric and complex-hermitian eigenvalue problems. We have made use of a so-called Lanczos-Arnoldi algorithm developed in the Department of Computational



and Applied Mathematics at Rice University.<sup>16</sup> Using this algorithm we have studied kernels with row dimensions of order 10,000.

To supplement our study of particle-particle eigenvalues we have also calculated a set of kernel eigenvalues for the particle-hole channels. These channels describe scattering of  $S = 0$  (charge density) and  $S = 1$  (magnetic) excitations. Several points are important to note in this regard. First of all, the FLEX calculation (and any Baym-Kadanoff approach<sup>17</sup>) lacks self-consistency at the two-particle level. For this reason the density and magnetic propagators which enter the one-particle self-energy are not the same as those obtained by functional differentiation of the self-energy with respect to an external field. The difference may be described in terms of “vertex corrections” to the bare density and magnetic matrix elements  $V_d$  and  $V_m$ . Within FLEX the simplest vertex corrections  $\Delta\Gamma_d$  and  $\Delta\Gamma_m$  have a form closely related to the singlet and triplet interactions  $\Delta\Gamma_s$  and  $\Delta\Gamma_t$ , i.e., they represent the exchange of *single* crossed-channel density and magnetic fluctuations. More complicated vertex corrections take the Aslamazov-Larkin (AL) form,<sup>18,19</sup> i.e., they describe the emission and re-absorption of *pairs* of fluctuations. For reasons described previously<sup>19</sup> we omit the AL corrections to  $\Delta\Gamma_d$  and  $\Delta\Gamma_m$  in the analysis which follows.

It is also important to re-emphasize at this point that the one-particle FLEX calculations described here and in EB assume the exchange of elementary particle-hole fluctuations, but not elementary particle-particle fluctuations. For this reason particle-particle fluctuation propagators do not appear in crossed-channel contributions to  $\Delta\Gamma_d$  and  $\Delta\Gamma_m$  below. In analogy with Equations (5) and (6) the spin-diagonalized particle-hole vertices (see Figure 8) may be written as follows:

$$\Gamma_d^{\text{ph}}(12; 34) = V_d(12; 34) - \frac{1}{2}\Phi_d(42; 31) - \frac{3}{2}\Phi_m(42; 31) \quad (28)$$

$$\Gamma_m^{\text{ph}}(12; 34) = V_m(12; 34) - \frac{1}{2}\Phi_d(42; 31) + \frac{1}{2}\Phi_m(42; 31). \quad (29)$$

The functions  $\Phi_d$  and  $\Phi_m$  are as defined previously.

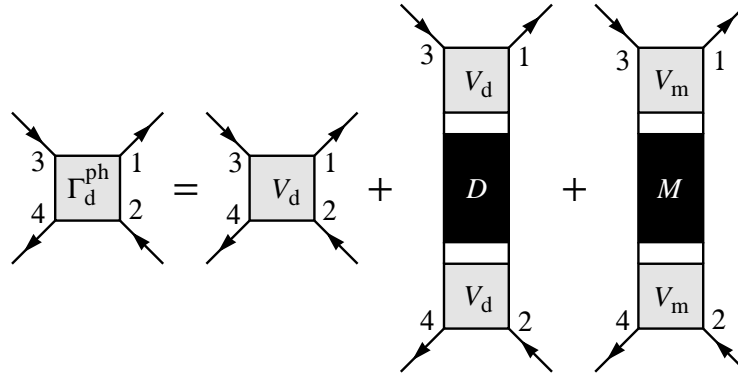


FIG. 8. Irreducible density vertex function  $\Gamma_d^{\text{ph}}$  within the FLEX approximation. Note the absence of AL and particle-particle exchange diagrams discussed in the text. (As before, the coefficients  $-1/2$  and  $-3/2$  are omitted for clarity; see Equation (28).)

In terms of the center-of-mass momentum-frequency  $Q$  the density vertex takes the form

$$\begin{aligned} \Gamma_d^{\text{ph}}(Q; m_1 m_2, \Delta\mathbf{R}_{12}, i\omega; m_3 m_4, \Delta\mathbf{R}_{34}, i\omega') = & \\ V_d(\mathbf{Q}; m_1 m_2, \Delta\mathbf{R}_{12}; m_3 m_4, \Delta\mathbf{R}_{34}) & \\ + \sum_{\Delta\mathbf{R}_{13}} e^{-i\mathbf{Q} \cdot \Delta\mathbf{R}_{13}} \Delta\Gamma_d^{\text{ph}}(\Delta\mathbf{R}_{13}, i\Omega; m_1 m_2, \Delta\mathbf{R}_{12}, i\omega; m_3 m_4, \Delta\mathbf{R}_{34}, i\omega'), & \end{aligned} \quad (30)$$

with

$$\begin{aligned} \Delta\Gamma_d^{\text{ph}}(\Delta\mathbf{R}_{13}, i\Omega; m_1 m_2, \Delta\mathbf{R}_{12}, i\omega; m_3 m_4, \Delta\mathbf{R}_{34}, i\omega') = & \\ \frac{1}{N} \sum_{\mathbf{Q}'} e^{i\mathbf{Q}' \cdot \Delta\mathbf{R}_{43}} \left[ -\frac{1}{2}\Phi_d - \frac{3}{2}\Phi_m \right](\mathbf{Q}', i(\omega' - \omega); m_4 m_2, \Delta\mathbf{R}_{42}; m_3 m_1, \Delta\mathbf{R}_{31}), & \end{aligned} \quad (31)$$

where, as in Equation (23), all relative displacements are expressed in terms of the set  $\{\Delta\mathbf{R}_{13}, \Delta\mathbf{R}_{12}, \Delta\mathbf{R}_{34}\}$ . The analogous expression for  $\Gamma_m^{\text{ph}}$  follows by the correspondence in Equation (29).

The particle-hole eigenvalue problem takes the form

$$\Gamma_r^{\text{ph}}(Q)G^{\text{ph}}(Q)\phi(Q) = \lambda(Q)\phi(Q) , \quad (32)$$

where now

$$G^{\text{ph}}(Q; m_1 m_2, \Delta \mathbf{R}_{12}, i\omega; m_3 m_4, \Delta \mathbf{R}_{34}, i\omega') = \delta_{\omega\omega'} \frac{T}{N} \sum_{\mathbf{k}} e^{i\mathbf{k} \cdot (\Delta \mathbf{R}_{12} - \Delta \mathbf{R}_{34})} G_{m_1 m_3}(k+Q) G_{m_4 m_2}(k) . \quad (33)$$

As in Equation (27), a positive eigenvalue indicates attraction.

## IV. RESULTS AND DISCUSSION

### A. Sources of Systematic Error

In this section we discuss the nature of the errors which arise in calculation of instability eigenvalues and transition temperatures. Four main sources of error arise in the eigenvalue calculations. These are accumulation of frequency-space renormalization group<sup>20</sup> error at low temperatures; error from the use of frequency cutoffs; error from truncation of the two-body vertex function in the relative real-space coordinate; and  $\mathbf{k}$ -space discretization error ( $16 \times 16$  meshes are employed throughout). Detailed discussions of the renormalization group procedure for the one-particle self-energy are included in EB and Reference 20. The errors associated with this approximation are generally negligibly small in comparison with the other sources.

The frequency cutoff used in our calculations is  $\Omega_c = 0.5t_{\text{pd}}$  for the ingoing and outgoing frequencies  $\omega$  and  $\omega'$  (see Figure 6) in the fluctuation-induced component of the singlet kernel. For the instantaneous part of the singlet kernel, whose decrease at high frequencies is controlled solely by the falloff of the uncorrelated propagator  $G^{\text{pp}}$ , the corresponding cutoff is  $50t_{\text{pd}}$ . Errors associated with these cutoffs are extremely small. For example, for the standard parameter set (see Equation (34)) at 16% hole doping and temperature  $T = t_{\text{pd}}/512$  (29 K), the  $d_{x^2-y^2}$  eigenvalue obtained using the cutoffs described above is  $\lambda_d = 1.0458$ . If both cutoffs are raised to  $50t_{\text{pd}}$ , the eigenvalue becomes 1.0459, a change of 0.01%; this demonstrates the calculation's insensitivity to the cutoff associated with the fluctuation component. In contrast, if both cutoffs are dropped to  $0.5t_{\text{pd}}$ , the eigenvalue becomes 1.0439, a change of 0.2%; this demonstrates insensitivity to the cutoff associated with the instantaneous component. It should be noted that at higher temperatures the cutoff on the fluctuation component must be raised to obtain comparable percentage accuracy. This is not costly, however, since the density of Matsubara frequencies decreases at the same time.

Next we discuss the truncation procedure for dealing with the relative real-space coordinate in the two-body vertex. When the kernels are evaluated on a  $16 \times 16$   $\mathbf{k}$ -space grid, the relative displacements  $\Delta \mathbf{R}_{12}$  and  $\Delta \mathbf{R}_{34}$  (see Figure 6) may take on 256 different values. Since the  $d_{x^2-y^2}$  eigenfunctions fall off rapidly at large values of  $\Delta \mathbf{R}_{12}$  (see Section IV D), it is rather intuitive to introduce a truncated basis set for the relative displacements. In our calculations we limit the basis set to the twenty-one smallest lattice vectors; i.e., elements of the kernel are zeroed out for  $|\Delta \mathbf{R}| > a\sqrt{5}$ . The corresponding gain in computation time is approximately  $(256/21)^2 \sim 150$ .

Since the calculation of the full model with the untruncated real-space basis set is too time-consuming to be practical, we have used the simpler model with  $U_{\text{pp}} = U_{\text{pd}} = 0$  for an error analysis. The behavior of the two models is expected to be identical as far as this error check is concerned. In Figure 9 we plot the temperature dependence of the  $d_{x^2-y^2}$  eigenvalue for the  $U_{\text{dd}}$ -only model using the untruncated basis set and the 21-state basis set. The difference in the eigenvalues is very small for the two cases. For example, at  $T = t_{\text{pd}}/1024$  (15 K),  $\lambda_d = 1.0683$  with the untruncated basis and  $\lambda_d = 1.0572$  with the 21-state basis. The corresponding  $T_c$  values are 20.8 K and 20.1 K, justifying the use of the truncated basis set.

The biggest source of error in the calculation of the instability eigenvalues is the use of a  $16 \times 16$   $\mathbf{k}$ -space discretization. For the models under study, the low-temperature eigenvalues from a  $16 \times 16$  and a  $32 \times 32$  discretization differ by less than 5%. This discretization error is very similar to that in previous studies of the one-band Hubbard model.<sup>19,21</sup> This means one should also expect roughly the same size error (i.e., 5%) in comparing the  $16 \times 16$  results to the fine-mesh limit.

In the figure below we plot the temperature dependence of the  $d_{x^2-y^2}$  eigenvalue for the  $U_{\text{dd}}$ -only model using  $16 \times 16$  and  $32 \times 32$  discretizations. (Essentially identical behavior is expected for the the full  $\text{CuO}_2$  model.) At  $T = t_{\text{pd}}/1024$  (15 K),  $\lambda_d = 1.1034$  for the  $32 \times 32$  study and 1.0572 for the  $16 \times 16$  study. For both cases a 21-state real-space basis truncation has been employed. The corresponding  $T_c$  values are 24 K and 20 K, corresponding to an underestimation of  $T_c$  by 4 K using the  $16 \times 16$  discretization.

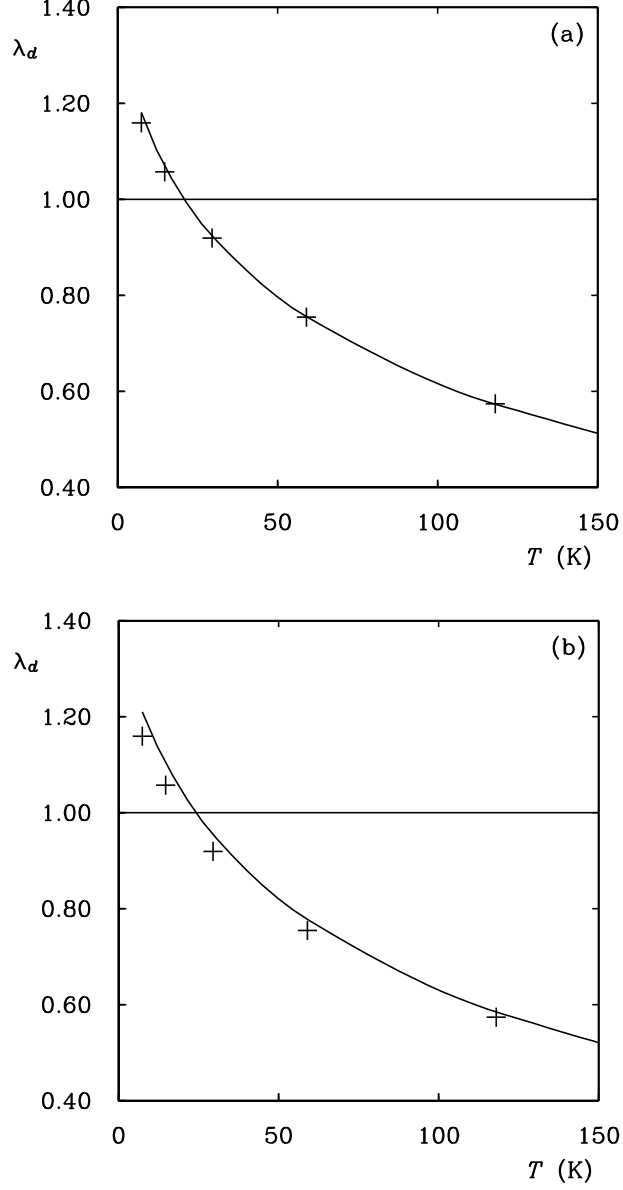


FIG. 9. Systematic error analysis for eigenvalue and  $T_c$  calculations in the  $U_{dd}$ -only model. All parameters are at their standard values (Equation (34)) except that  $U_{pp} = U_{pd} = 0$ . The filling is  $\langle n \rangle = 1.16$ . (a) Comparison of temperature-dependent  $d_{x^2-y^2}$  eigenvalues calculated using a full basis of relative displacement states (solid line) and the 21-state basis with  $|\Delta \mathbf{R}| \leq a\sqrt{5}$  (crosses). The  $\mathbf{k}$ -space mesh is  $16 \times 16$ . (b) Comparison of eigenvalues calculated using a  $32 \times 32$  discretization (solid line) and a  $16 \times 16$  discretization (crosses). The 21-state truncated basis is employed.

As mentioned in Section III we have employed a Lanczos-Arnoldi algorithm<sup>16</sup> to calculate the first few maximum-real-part eigenvalues in each scattering channel. This algorithm is especially powerful for sparse matrices because it requires only repetitive multiplication of a vector by the matrix of interest. Since a large fraction of the elements in our scattering kernels are non-zero, but negligibly small with regard to calculation of the large eigenvalues, a sparse storage scheme is appropriate. For the scheme adopted throughout most of our calculations, eigenvalues are affected by less than a few parts in a thousand, and the gain in storage is of order 50.

### B. Eigenvalues for Particle-Particle Channels

In the plots which follow we make use of a “standard” CuO<sub>2</sub> parameter set derived for undoped La<sub>2</sub>CuO<sub>4</sub> by Hybertsen, Schlüter, and Christensen<sup>9</sup> using constrained-occupancy density functional theory. These standard parameters for the Hamiltonian in Equations (1) and (2) are as follows:

$$\begin{aligned}
 t_{\text{pd}} &\simeq 1.3 \text{ eV} = 15,100 \text{ K} \\
 t_{\text{pp}} &\simeq 0.65 \text{ eV} = 0.5t_{\text{pd}} \\
 \varepsilon &\simeq 3.6 \text{ eV} = 2.75t_{\text{pd}} \\
 U_{\text{dd}} &\simeq 10.5 \text{ eV} = 8t_{\text{pd}} \\
 U_{\text{pp}} &\simeq 4 \text{ eV} = 3t_{\text{pd}} \\
 U_{\text{pd}} &\simeq 1.2 \text{ eV} = t_{\text{pd}} .
 \end{aligned} \tag{34}$$

The temperature dependence of the maximal particle-particle eigenvalues for the standard parameter set at  $\langle n \rangle = 1.16$  (16% hole doping) is illustrated in Figure 10. The maximal singlet eigenvalue corresponds to a  $d_{x^2-y^2}$  state. This eigenvalue reaches unity, indicating a superconducting transition, at  $T/t_{\text{pd}} = 0.0025$ , i.e.,  $T = 37 \text{ K}$ . At the transition temperature the next-leading singlet eigenvalue is of order 0.4 and corresponds to a state with so-called g-wave symmetry (i.e., nodes on the  $x$  and  $y$  axes, as well as the lines  $x = \pm y$ ; see Figure 11). A third eigenvalue, corresponding to an orthogonal  $d_{x^2-y^2}$  state, lies just below the g-wave.

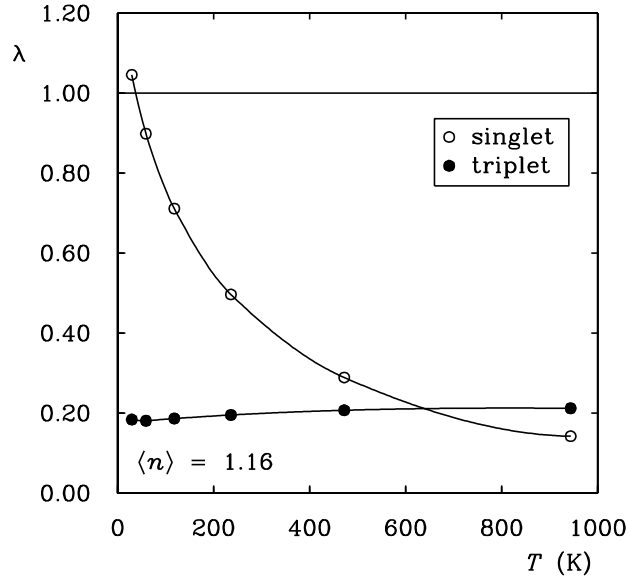


FIG. 10. Temperature dependence of the maximal singlet and triplet eigenvalues for the standard parameter set at  $\langle n \rangle = 1.16$ . The singlet eigenfunction has  $d_{x^2-y^2}$  symmetry, and the triplet state odd-frequency s-wave symmetry. The  $d_{x^2-y^2}$  eigenvalue reaches unity, signaling a superconducting transition, at  $T = 37 \text{ K}$ .

The maximal triplet channel eigenvalue in Figure 10 remains small ( $\sim 0.2$ ) throughout the temperature range of interest. The triplet state in this case is antisymmetric in frequency and s-wave-like (i.e., symmetric) in space. (Note in this regard that our instability analysis includes all eigenvectors of the scattering kernels, including exotic singlet and triplet states with an antisymmetric frequency dependence.)

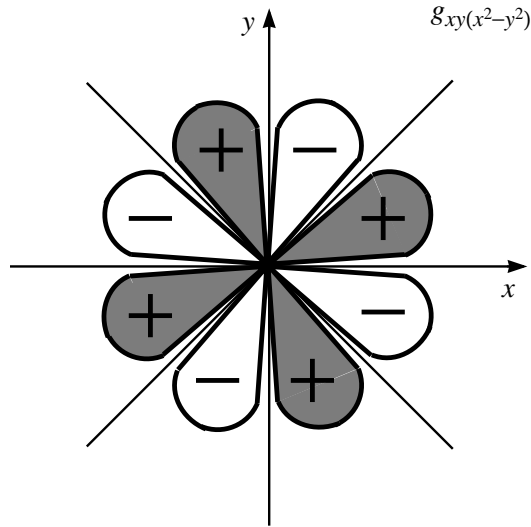


FIG. 11. Schematic representation of the nodal structure of the  $g_{xy(x^2-y^2)}$  singlet state. Note that the subscript, when viewed as a function, vanishes on the locus of nodes (just as in the case of the  $d_{x^2-y^2}$  state).

For comparison the behavior of the maximal particle-particle eigenvalues at  $\langle n \rangle = 1.00$  is illustrated in Figure 12. The extreme singularity of the magnetic fluctuations in this case prevents study at temperatures lower than  $t_{pd}/64$ , i.e.,  $T = 240$  K.

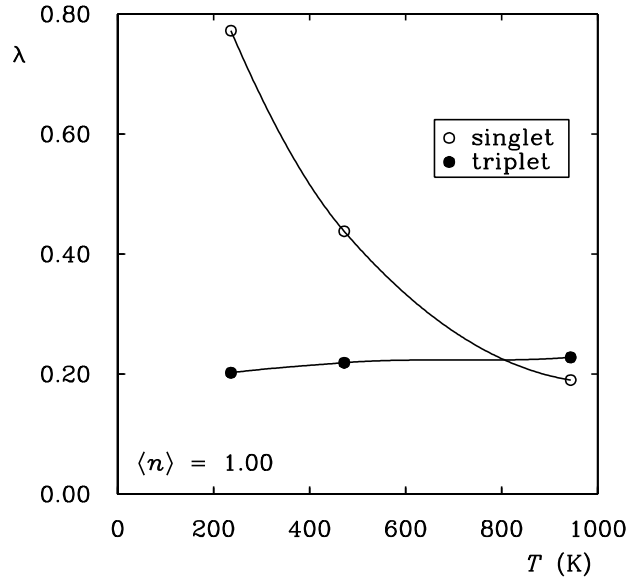


FIG. 12. Temperature dependence of the maximal singlet and triplet eigenvalues for the standard parameter set at  $\langle n \rangle = 1.00$ . The eigenfunction symmetries are as in Figure 10.

### C. Transition Temperatures for $d_{x^2-y^2}$ Superconductivity

Eigenvalue plots of the type illustrated in Figure 10 may be used to extract transition temperatures for the  $d_{x^2-y^2}$  singlet. The critical behavior of this FLEX transition is classical, despite the fact that it is driven entirely by fluctuations. In terms of the FLEX eigenvalues,

$$\lambda_d(T) \sim 1 - a(T - T_c) \quad (35)$$

for  $T \sim T_c$ , with  $a > 0$ . This contrasts with the exact critical behavior for a two-dimensional superconducting transition in the xy universality class:

$$\lambda_{xy}(T) \sim 1 - B(T)e^{-A/\sqrt{T-T_{xy}}}, \quad (36)$$

with  $A$  a positive constant and  $B(T)$  an algebraic function.<sup>22</sup> It is nevertheless possible to interpret the  $d_{x^2-y^2}$  instability in FLEX as a “mean-field” transition with respect to critical order parameter fluctuations. With this caveat it is of interest to examine the dependence of this instability on doping and model parameters. [A more sophisticated treatment of the interference between the  $d_{x^2-y^2}$  transition and the incipient instability in the magnetic channel is presumably necessary for a detailed understanding of the pseudogap regime observed in experiments,<sup>23</sup> but that is not our intention here. In fact an additional charge density state, the so-called “orbital antiferromagnet”<sup>24</sup> or “flux phase,”<sup>25</sup> is also apparently relevant in the pseudogap regime; see the discussion of this state in Section IV E.]

In the plots which follow transition temperatures are given in units of K; they may be rescaled in units of  $t_{pd}$  using the correspondence in Equation (34). The experimentally observed transition temperatures<sup>26</sup> for  $\text{La}_{2-x}\text{Sr}_x\text{CuO}_4$  are plotted for comparison using the assumed correspondence

$$x \rightarrow \langle n \rangle - 1. \quad (37)$$

As shown in Figure 13, a  $d_{x^2-y^2}$  transition occurs for both hole doping ( $\langle n \rangle$  greater than 1) and electron doping ( $\langle n \rangle$  less than 1). Since the  $\text{CuO}_2$  model has only approximate particle-hole symmetry around the point  $\langle n \rangle = 1$ , the

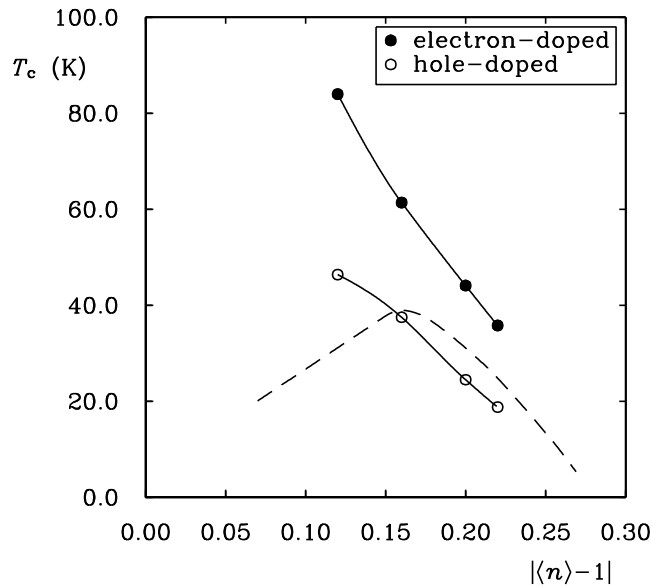


FIG. 13. Doping dependence of the  $d_{x^2-y^2}$  transition for the standard parameter set. Results are shown for both  $\langle n \rangle > 1.00$  (hole doping) and  $\langle n \rangle < 1.00$  electron doping. For comparison the doping dependence of the experimental transition<sup>26</sup> in  $\text{La}_{2-x}\text{Sr}_x\text{CuO}_4$  is plotted (dashed line) using the assumed correspondence  $x \rightarrow \langle n \rangle - 1$ . The increase of the FLEX  $T_c$  on the electron-doped side is largely due to an increase in the spin fluctuation strength.

transition temperatures are not symmetric. Within our FLEX calculation the pairing interaction becomes increasingly singular as  $\langle n \rangle \rightarrow 1$ , and we have only been able to calculate superconducting instability temperatures for doping levels greater than 12%. (In any case a self-consistent parquet-like treatment of vertex functions<sup>14,19</sup> seems essential for values of  $\langle n \rangle$  closer to unity.) The higher transitions for electron doping are consistent with the presence of enhanced magnetic fluctuations on this side of the phase diagram.<sup>12,13</sup> The transition temperatures on the hole-doped side are strikingly similar to the experimental curve in the overdoped regime,  $\langle n \rangle - 1 > 0.16$ . At smaller doping the FLEX curve continues to rise, while the experimental curve peaks and turns down in the underdoped region. As remarked previously, in this region the  $d_{x^2-y^2}$  singlet channel is in strong competition with the  $\mathbf{Q} \sim (\pi, \pi)$  antiferromagnetic spin channel, as well as an exotic  $\mathbf{Q} \sim (\pi, \pi)$  charge density channel (see also Section IV E). It is tempting to speculate that the downturn in the experimental  $d_{x^2-y^2}$  transition temperature results from this competition.

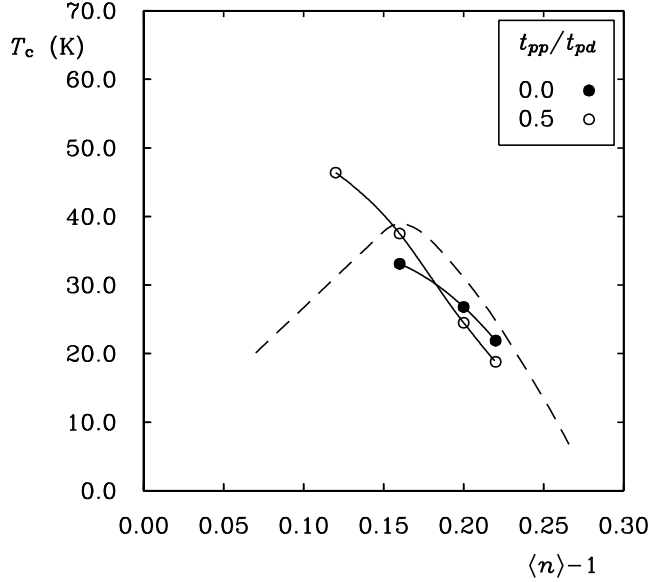


FIG. 14. Dependence of  $T_c$  on the O–O hopping integral  $t_{pp}$ . In Figures 14–19 all model parameters are set to their standard values except as noted. Further the experimental curve<sup>26</sup> for doped lanthanum cuprate (dashed line) is superimposed for comparison.

In the next six figures we examine the sensitivity of the  $d_{x^2-y^2}$  transition temperature to changes in the model parameters. Our discussion is limited to the hole-doped side of the phase diagram. First we alter a single parameter at a time, keeping other parameters fixed at their standard values, then we briefly consider the behavior of the drastically simplified  $\text{CuO}_2$  model with  $U_{pp} = U_{pd} = 0$ .

The effect of removing the O–O hopping integral  $t_{pp}$  is shown in Figure 14. This change alters the shape of the Fermi surface,<sup>12</sup> improving the degree of nesting and enhancing the spin fluctuation spectrum. However, the transition temperature remains essentially unchanged, since the positive effect on the singlet vertex is largely compensated by a reduction in the uncorrelated propagator  $G^{PP}$ .

The effect of changing the Cu–O orbital separation  $\varepsilon = \varepsilon_p - \varepsilon_d$  is much more drastic, as expected. The value of  $\varepsilon$  largely determines the strength of the spin fluctuations. (This is because  $\varepsilon$  is smaller than  $U_{dd}$ , i.e., the system is in the so-called charge-transfer regime.<sup>7</sup>) For small values of  $\varepsilon$ , occupation of the O orbitals becomes comparable to occupation of the Cu orbitals (or even larger, when Coulomb interactions are taken into account). As an example, for  $\varepsilon = 0$  and  $\langle n \rangle = 1.16$ , only 33% of the holes reside on the Cu orbitals. Since  $U_{pp}$  is considerably less than  $U_{dd}$ , increased O occupancy reduces the strength of the spin fluctuation propagator and weakens the pairing tendency. This fact is illustrated clearly in Figure 15. The  $d_{x^2-y^2}$  transition temperature drops sharply when  $\varepsilon$  is reduced from 3.6 eV to 2.0 eV. The transition disappears completely when  $\varepsilon$  is set to zero (i.e., the bare Cu and O orbitals become degenerate); this is due not only to the reduction of the effective Coulomb parameter, but also to the loss of nesting in the  $\varepsilon = 0$  Fermi surface.

The dependence of  $T_c$  on the Coulomb parameters  $U_{dd}$ ,  $U_{pp}$ , and  $U_{pd}$  is relatively complex, since these parameters contribute to both the one- and two-body effective interactions. For the simpler one-band Hubbard model<sup>21</sup> (and for the  $\text{CuO}_2$  model with  $U_{dd}$  only—see the discussion below), an increase of the Coulomb integral leads to a peak  $T_c$ , then a gradual decrease at larger values. The origin of this behavior is a competition between the pairing vertex (which is enhanced by a large Coulomb interaction) and the uncorrelated propagator  $G^{PP}$  (which is suppressed). In these simpler models the on-site Coulomb interaction does not *directly* suppress pairing, since the  $d_{x^2-y^2}$  state has no on-site pairing component. While this remains true for  $U_{dd}$  in the full  $\text{CuO}_2$  model, it is not necessarily true for  $U_{pp}$  and  $U_{pd}$ : the  $d_{x^2-y^2}$  pair wave function generally has on-site O–O and near-neighbor Cu–O components, which are suppressed by the Coulomb integrals  $U_{pp}$  and  $U_{pd}$ . The importance of this direct effect depends on the admixture of the relevant components in the  $d_{x^2-y^2}$  pair state (see the discussion of the pair wave function in Section IV D).

For the O–O Coulomb integral  $U_{pp}$ , this direct suppression of pairing apparently dominates, i.e., an increase in  $U_{pp}$  leads to more repulsion in the  $d_{x^2-y^2}$  pair state and a reduced transition temperature (Figure 16). As discussed in Section IV D below, the  $d_{x^2-y^2}$  pair does have a non-zero on-site O–O component, consistent with the observed trend in  $T_c$ .

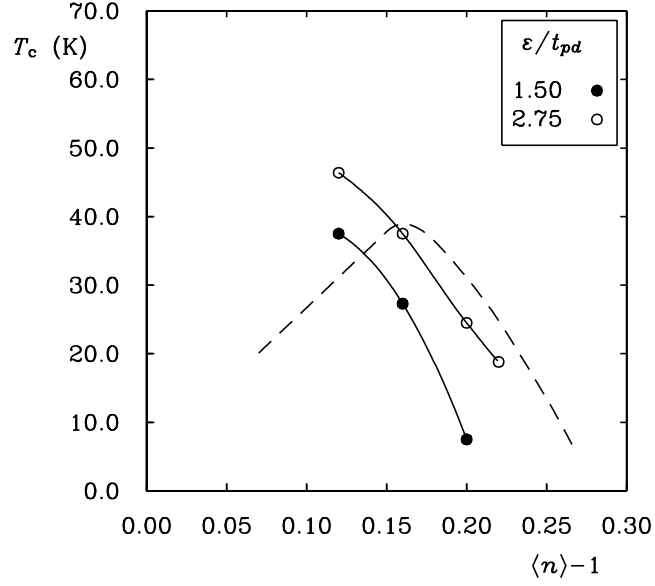


FIG. 15. Dependence of  $T_c$  on the unrenormalized Cu-O level separation  $\varepsilon = \varepsilon_p - \varepsilon_d$ . The behavior of the model for  $\varepsilon = 0$  was also examined, but no transition occurs in this case.

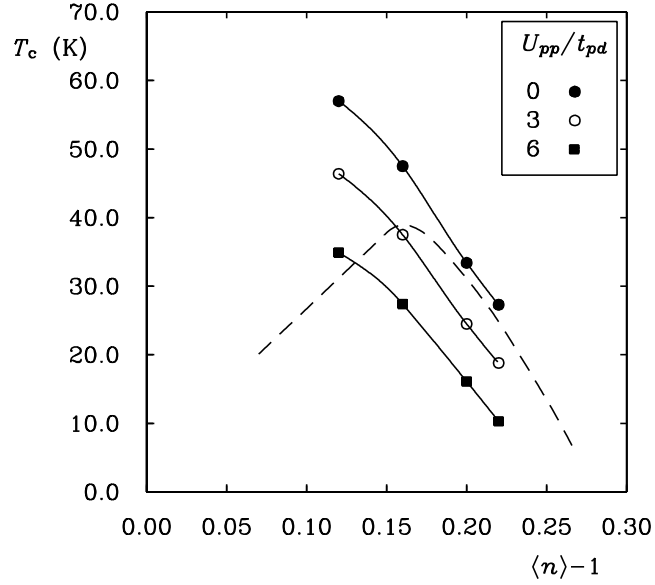


FIG. 16. Dependence of  $T_c$  on the intra-orbital O-O Coulomb integral  $U_{pp}$ .



For the Cu–O Coulomb integral  $U_{pd}$ , the trend in  $T_c$  with increasing  $U_{pd}$  (Figure 17) resembles the trend with increasing  $U$  in the one-band Hubbard model: An increase, peak, and subsequent decrease. This behavior reflects

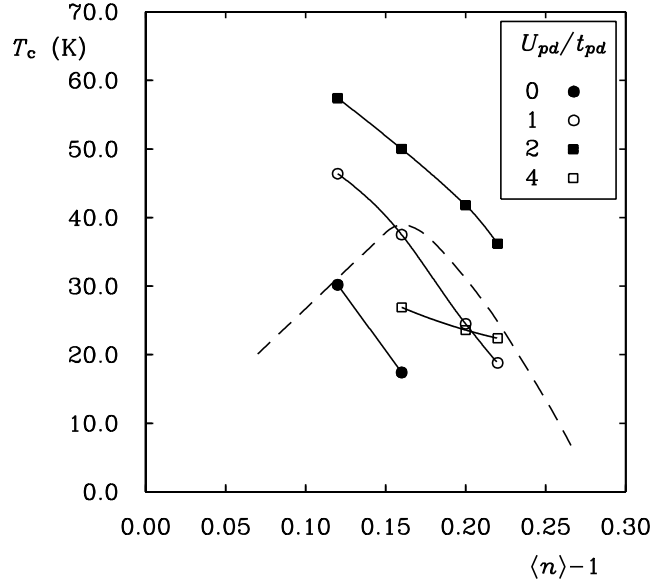


FIG. 17. Dependence of  $T_c$  on the near-neighbor Cu–O Coulomb integral  $U_{pd}$ .

a compromise between the enhancement of the spin fluctuations and pairing interaction with increased  $U_{pd}$ ; the accompanying suppression of  $G^{PP}$ ; and the direct suppression of  $T_c$  noted above. The enhancement of the spin fluctuations with increasing  $U_{pd}$  arises from improved Fermi surface nesting and from increased d-orbital occupancy due to a rise in the Hartree-Fock level separation  $\varepsilon_{HF}$  (see the discussion of the Hartree-Fock Hamiltonian in EB). [It is interesting to note that the direct suppression of  $T_c$  is moderated by the same phenomenon which reduces the effective Coulomb repulsion in conventional electron-phonon superconductivity:<sup>27</sup> The near-neighbor component of the pair wave function changes sign at high frequencies, effectively reducing the repulsion in the low-frequency region, i.e., inducing a Coulomb pseudopotential.]

Finally Figure 18 shows the transition temperatures for two different values of  $U_{dd}$ , 10.5 eV (standard parameter set—charge-transfer regime) and 2.5 eV (Hubbard regime). The substantial reduction in  $U_{dd}$  in this case has only a minimal effect on the strength of the spin fluctuations.<sup>12</sup> This is because a *decrease* in  $U_{dd}$  results in an increased Hartree-Fock level separation  $\varepsilon_{HF}$  and an increased d-orbital occupancy (cf. the discussion of an *increase* in  $U_{pd}$  above). The increased d-orbital occupancy offsets the direct effect of a smaller  $U_{dd}$  in the spin fluctuation propagator. The increase in  $T_c$  for this admittedly unrealistic parameter set then results from an increase in  $G^{PP}$  (i.e., a density of states effect).

The  $\text{CuO}_2$  model with  $U_{pp} = U_{pd} = 0$  (the “ $U_{dd}$ -only model”) has been studied previously<sup>13</sup> at temperatures above the  $d_{x^2-y^2}$  transition. This model is conceptually problematic: the omission of the interactions associated with the p-orbitals substantially alters the Hartree-Fock Fermi surface, largely negating any improvement in the band structure expected from the addition of the extra bands. (Both  $G^{PP}$  and the d-orbital spin fluctuation strength are significantly affected by the omission.) Furthermore, while the  $d_{x^2-y^2}$  wave function is dominated by d-orbital components, the omission of  $U_{pp}$  and  $U_{pd}$  completely eliminates those components associated with the p-orbitals. The principal virtue of the  $U_{dd}$ -only model is its calculational simplicity. Since the Coulomb interaction  $U_{dd}$  is zero-range, the computations involved are essentially the same as those in the one-band Hubbard model. For example, the particle-hole ladders  $\Phi$  in Section III become scalar, rather than matrix, inverses.

For completeness, the variation of  $T_c$  with  $U_{dd}$  in the  $U_{dd}$ -only model is shown in Figure 19. As expected, the qualitative dependence of  $T_c$  is the same as that in the one-band Hubbard model:<sup>21</sup> The peak value of  $T_c$  for increasing  $U_{dd}$  is determined by a competition between enhancement of the pairing interaction and suppression of the uncorrelated propagator  $G^{PP}$ .

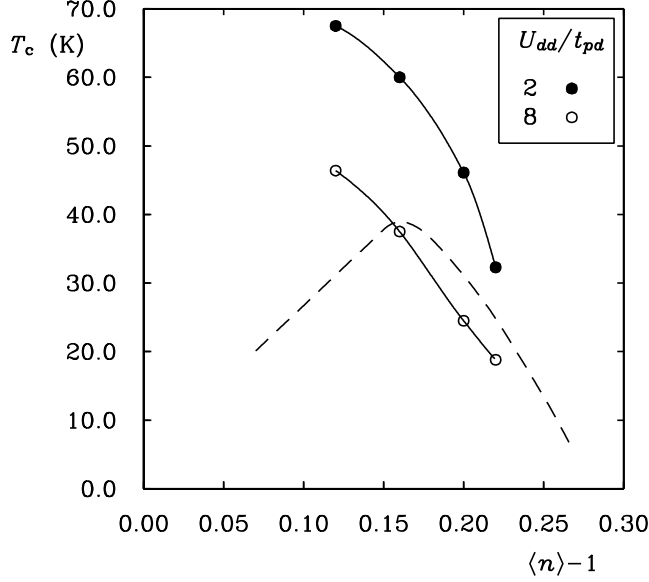


FIG. 18. Dependence of  $T_c$  on the intra-orbital Cu–Cu Coulomb integral  $U_{dd}$ .

#### D. $d_{x^2-y^2}$ Singlet Wave Function

The graphical representation of the particle-particle pair eigenfunction  $\phi(Q; ab, \Delta \mathbf{R}_{ab}, i\omega)$  is hindered by its large number of degrees of freedom. It is essential to make use of symmetries to emphasize the eigenfunction's key features. The first basic symmetry follows from the Pauli Principle. Written in terms of anticommuting c-numbers, the pair state corresponding to eigenfunction  $\phi_r$  is

$$\begin{aligned} & \sum_{\mathbf{R}; ab, \Delta \mathbf{R}_{ab}, \omega} e^{i\mathbf{Q} \cdot (\mathbf{R} + \Delta \mathbf{R}_{ab})} \phi_r(Q; ab, \Delta \mathbf{R}_{ab}, i\omega) \\ & \times \sum_{\sigma\sigma'} \chi_r^{\sigma\sigma'} \bar{c}_{a\sigma}(\mathbf{R} + \Delta \mathbf{R}_{ab}, i(\omega + \Omega)) \bar{c}_{b\sigma'}(\mathbf{R}, -i\omega), \end{aligned} \quad (38)$$

where  $r=s$  or  $t$ , with

$$\chi_s = \frac{1}{\sqrt{2}} \begin{pmatrix} 0 & 1 \\ -1 & 0 \end{pmatrix} \quad (39)$$

and

$$\chi_t = \begin{pmatrix} 1 & 0 \\ 0 & 0 \end{pmatrix}, \quad \frac{1}{\sqrt{2}} \begin{pmatrix} 0 & 1 \\ 1 & 0 \end{pmatrix}, \quad \text{or} \quad \begin{pmatrix} 0 & 0 \\ 0 & 1 \end{pmatrix}. \quad (40)$$

Since

$$\bar{c}_{a\sigma} \bar{c}_{b\sigma'} = -\bar{c}_{b\sigma'} \bar{c}_{a\sigma}, \quad (41)$$

it follows that

$$\begin{aligned} & \sum_{\mathbf{R}; ab, \Delta \mathbf{R}_{ab}, \omega} e^{i\mathbf{Q} \cdot (\mathbf{R} + \Delta \mathbf{R}_{ab})} \phi_r(Q; ab, \Delta \mathbf{R}_{ab}, i\omega) \\ & \times \sum_{\sigma\sigma'} \chi_r^{\sigma'\sigma} \bar{c}_{b\sigma}(\mathbf{R}, -i\omega) \bar{c}_{a\sigma'}(\mathbf{R} + \Delta \mathbf{R}_{ab}, i(\omega + \Omega)) = \\ & \sum_{\mathbf{R}; ab, \Delta \mathbf{R}_{ab}, \omega} e^{i\mathbf{Q} \cdot (\mathbf{R} + \Delta \mathbf{R}_{ab})} \phi_r(Q; ab, \Delta \mathbf{R}_{ab}, i\omega) \\ & \times \sum_{\sigma\sigma'} \chi_r^{\sigma\sigma'} \bar{c}_{a\sigma}(\mathbf{R} + \Delta \mathbf{R}_{ab}, i(\omega + \Omega)) \bar{c}_{b\sigma'}(\mathbf{R}, -i\omega). \end{aligned} \quad (42)$$

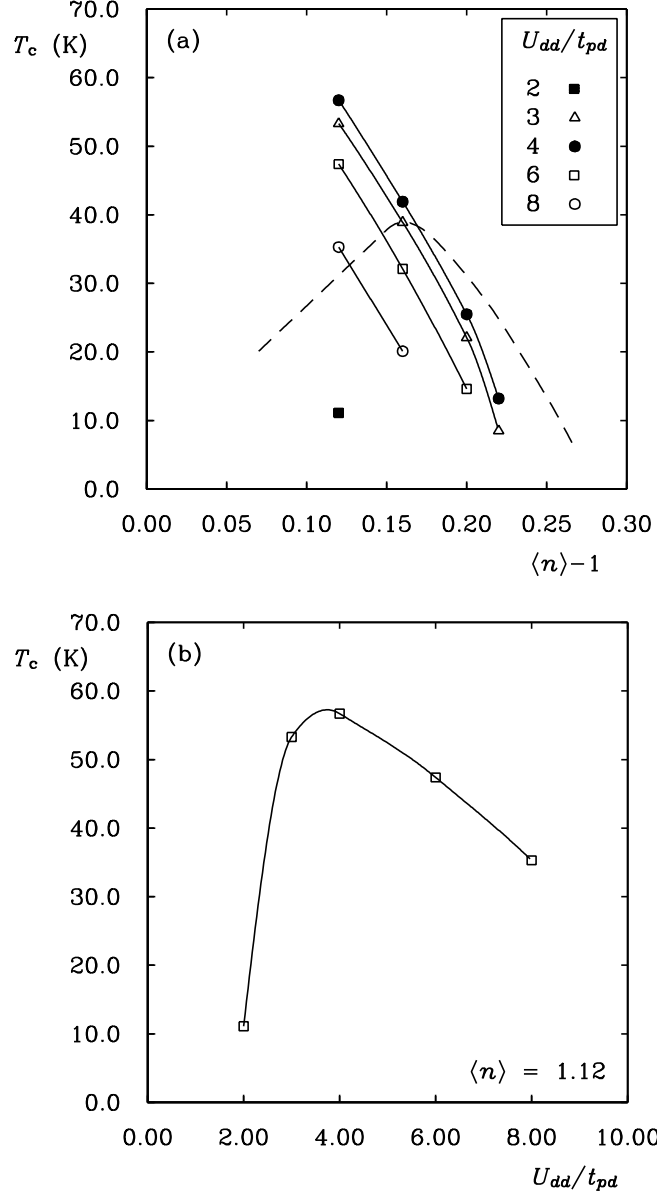


FIG. 19. Dependence of  $T_c$  on the intra-orbital Cu-Cu Coulomb integral  $U_{dd}$  in the “ $U_{dd}$ -only” model. The Coulomb integrals  $U_{pp}$  and  $U_{pd}$  are in this case set to zero, with other parameters remaining at their standard values. (a) Variation of  $T_c$  with doping for several values of  $U_{dd}$ . The behavior for  $U_{dd}/t_{pd} = 1$  was also examined, but no transition occurs in this case. (b) Variation of  $T_c$  with  $U_{dd}$  at fixed filling  $\langle n \rangle = 1.12$ .

It is convenient to relabel the dummy sums on the left by first interchanging orbital indices  $a$  and  $b$ , then letting

$$\begin{aligned}\Delta\mathbf{R}_{ba} &= -\Delta\mathbf{R}_{ab} \\ \mathbf{R} &= \mathbf{R}' + \Delta\mathbf{R}_{ab} \\ -i\omega &= i(\omega' + \Omega) .\end{aligned}\tag{43}$$

Dropping the primes on the dummy variables  $\mathbf{R}'$  and  $\omega'$  gives

$$\begin{aligned}& \sum_{\mathbf{R}; ab, \Delta\mathbf{R}_{ab}, \omega} e^{i\mathbf{Q}\cdot\mathbf{R}} \phi_r(Q; ba, -\Delta\mathbf{R}_{ab}, -i(\omega + \Omega)) \\ & \times \sum_{\sigma\sigma'} \chi_r^{\sigma'\sigma} \bar{c}_{a\sigma}(\mathbf{R} + \Delta\mathbf{R}_{ab}, i(\omega + \Omega)) \bar{c}_{b\sigma'}(\mathbf{R}, -i\omega) = \\ & - \sum_{\mathbf{R}; ab, \Delta\mathbf{R}_{ab}, \omega} e^{i\mathbf{Q}\cdot(\mathbf{R}+\Delta\mathbf{R}_{ab})} \phi_r(Q; ab, \Delta\mathbf{R}_{ab}, i\omega) \\ & \times \sum_{\sigma\sigma'} \chi_r^{\sigma\sigma'} \bar{c}_{a\sigma}(\mathbf{R} + \Delta\mathbf{R}_{ab}, i(\omega + \Omega)) \bar{c}_{b\sigma'}(\mathbf{R}, -i\omega) .\end{aligned}\tag{44}$$

The Pauli symmetry relations follow by identifying coefficients:

$$\phi_r(Q; ba, -\Delta\mathbf{R}_{ab}, -i(\omega + \Omega)) \chi_r^{\sigma'\sigma} = -e^{i\mathbf{Q}\cdot\Delta\mathbf{R}_{ab}} \phi_r(Q; ab, \Delta\mathbf{R}_{ab}, i\omega) \chi_r^{\sigma\sigma'} ,\tag{45}$$

i.e.,

$$\phi_s(Q; ab, \Delta\mathbf{R}_{ab}, i\omega) = e^{-i\mathbf{Q}\cdot\Delta\mathbf{R}_{ab}} \phi_s(Q; ba, -\Delta\mathbf{R}_{ab}, -i(\omega + \Omega))\tag{46}$$

for the singlet channel, and

$$\phi_t(Q; ab, \Delta\mathbf{R}_{ab}, i\omega) = -e^{-i\mathbf{Q}\cdot\Delta\mathbf{R}_{ab}} \phi_t(Q; ba, -\Delta\mathbf{R}_{ab}, -i(\omega + \Omega))\tag{47}$$

for the triplet channel. These symmetry relations assume a particularly simple form for the case of interest here,  $Q = 0$ .

To aid in the graphical display of the pair wave function it is useful to introduce a basis of one-particle states with simple transformation properties under point group operations. While the Cu  $3d_{x^2-y^2}$  orbital transforms into itself under all symmetry operations, the O  $2p_x$  and  $2p_y$  orbitals are generally mixed. It is, however, possible to form linear combinations of the  $p_x$  and  $p_y$  orbitals which transform in simple ways. To derive the transformed orbitals we rewrite the pair wave function  $\phi$  in Equation (38), holding the coordinates of particle  $a$  fixed. For brevity the spin and frequency dependence of  $\phi$  is temporarily suppressed. The components of the wave function for  $b = x$  and  $y$  take the form

$$\begin{aligned}& \sum_{\mathbf{R}; a, \Delta\mathbf{R}_{ab}, \omega} e^{i\mathbf{Q}\cdot(\mathbf{R}+\Delta\mathbf{R}_{ab})} \bar{c}_a(\mathbf{R} + \Delta\mathbf{R}_{ab}) \\ & \times \left[ \phi_r(Q; ax, \Delta\mathbf{R}_{ab}) \bar{c}_x(\mathbf{R}) + \phi_r(Q; ay, \Delta\mathbf{R}_{ab}) \bar{c}_y(\mathbf{R}) \right] .\end{aligned}\tag{48}$$

In the first term the sums on  $\mathbf{R}$  and  $\Delta\mathbf{R}_{ab}$  may be shifted by

$$\begin{aligned}\mathbf{R} &\rightarrow \mathbf{R} - \hat{x} \\ \Delta\mathbf{R}_{ab} &\rightarrow \Delta\mathbf{R}_{ab} + \hat{x} .\end{aligned}\tag{49}$$

A similar shift may be performed in the second term with  $\hat{x} \rightarrow \hat{y}$ . This results in an equivalent symmetrized version of the wave function,

$$\begin{aligned}& \frac{1}{2} \sum_{\mathbf{R}; a, \Delta\mathbf{R}_{ab}, \omega} e^{i\mathbf{Q}\cdot(\mathbf{R}+\Delta\mathbf{R}_{ab})} \bar{c}_a(\mathbf{R} + \Delta\mathbf{R}_{ab}) \\ & \times \left[ \phi_r(Q; ax, \Delta\mathbf{R}_{ab}) \bar{c}_x(\mathbf{R}) + \phi_r(Q; ax, \Delta\mathbf{R}_{ab} + \hat{x}) \bar{c}_x(\mathbf{R} - \hat{x}) \right. \\ & \left. + \phi_r(Q; ay, \Delta\mathbf{R}_{ab}) \bar{c}_y(\mathbf{R}) + \phi_r(Q; ay, \Delta\mathbf{R}_{ab} + \hat{y}) \bar{c}_y(\mathbf{R} - \hat{y}) \right]\end{aligned}\tag{50}$$

The four c-numbers  $\bar{c}_x(\mathbf{R})$ ,  $\bar{c}_x(\mathbf{R} - \hat{x})$ ,  $\bar{c}_y(\mathbf{R})$ ,  $\bar{c}_y(\mathbf{R} - \hat{y})$  may now be re-expressed in terms of the linear combinations

$$\begin{bmatrix} \bar{c}_D(\mathbf{R}) \\ \bar{c}_S(\mathbf{R}) \\ \bar{c}_X(\mathbf{R}) \\ \bar{c}_Y(\mathbf{R}) \end{bmatrix} = \begin{bmatrix} 1/2 & 1/2 & 1/2 & 1/2 \\ 1/2 & 1/2 & -1/2 & -1/2 \\ 1/\sqrt{2} & -1/\sqrt{2} & 0 & 0 \\ 0 & 0 & -1/\sqrt{2} & 1/\sqrt{2} \end{bmatrix} \begin{bmatrix} \bar{c}_x(\mathbf{R}) \\ \bar{c}_x(\mathbf{R} - \hat{x}) \\ \bar{c}_y(\mathbf{R}) \\ \bar{c}_y(\mathbf{R} - \hat{y}) \end{bmatrix}. \quad (51)$$

The c-number  $\bar{c}_D(\mathbf{R})$  represents an extended oxygen orbital with  $d_{x^2-y^2}$  rotational symmetry (Figure 20(a)), just like the central Cu  $3d_{x^2-y^2}$  orbital. (The uniform phases in the linear combination result from the initial definition of the  $2p_x$  and  $2p_y$  orbitals.) Likewise  $\bar{c}_S(\mathbf{R})$  represents an extended s-wave oxygen orbital (Figure 20(b)), and  $\bar{c}_X(\mathbf{R})$  and  $\bar{c}_Y(\mathbf{R})$  represent extended p-wave orbitals (Figures 20(c) and (d)). The wave function components in Equation (50)

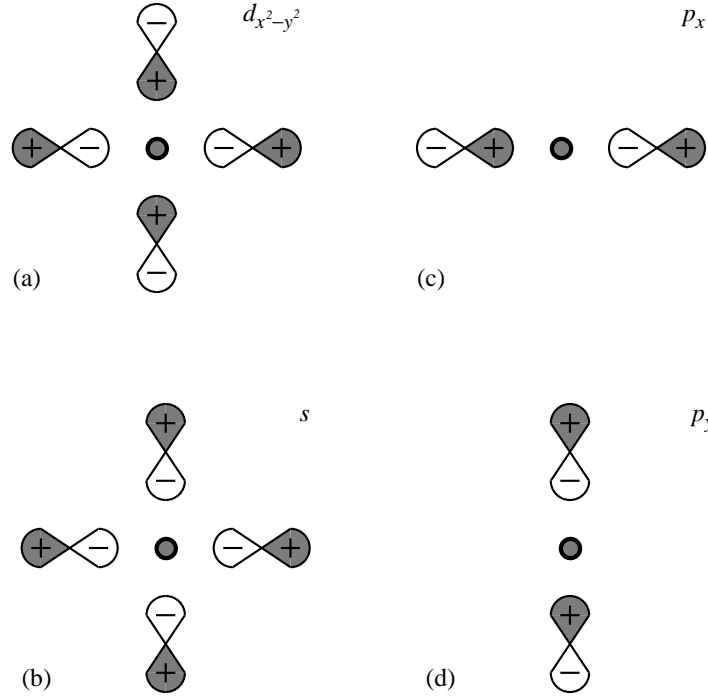


FIG. 20. Extended p-orbital basis set with well-defined rotational symmetry. The central Cu site is denoted by a shaded circle. (a) Extended  $d_{x^2-y^2}$  orbital (state  $D$ ). (b) Extended s orbital (state  $S$ ). (c) Extended  $p_x$  orbital (state  $X$ ). (d) Extended  $p_y$  orbital (state  $Y$ ).

may now be rewritten in terms of the new c-numbers. The complete pair wave function in Equation (38) then becomes

$$\begin{aligned} & \sum_{\mathbf{R}; aB, \Delta\mathbf{R}_{ab}, \omega} e^{i\mathbf{Q} \cdot (\mathbf{R} + \Delta\mathbf{R}_{ab})} \phi_r(Q; aB, \Delta\mathbf{R}_{ab}, i\omega) \\ & \times \sum_{\sigma\sigma'} \chi_r^{\sigma\sigma'} \bar{c}_{a\sigma}(\mathbf{R} + \Delta\mathbf{R}_{ab}, i(\omega + \Omega)) \bar{c}_{B\sigma'}(\mathbf{R}, -i\omega), \end{aligned} \quad (52)$$

where, as before, the sum on  $a$  runs over  $\{d, x, y\}$ , but now the sum on  $B$  runs over  $\{d, D, S, X, Y\}$ . The new wave function components are

$$\begin{aligned} \phi_r(Q; aD, \Delta\mathbf{R}_{ab}, i\omega) &= \\ & \frac{1}{4} \left[ \phi_r(Q; ax, \Delta\mathbf{R}_{ab}, i\omega) + \phi_r(Q; ax, \Delta\mathbf{R}_{ab} + \hat{x}, i\omega) \right. \\ & \left. + \phi_r(Q; ay, \Delta\mathbf{R}_{ab}, i\omega) + \phi_r(Q; ay, \Delta\mathbf{R}_{ab} + \hat{y}, i\omega) \right] \\ \phi_r(Q; aS, \Delta\mathbf{R}_{ab}, i\omega) &= \\ & \frac{1}{4} \left[ \phi_r(Q; ax, \Delta\mathbf{R}_{ab}, i\omega) + \phi_r(Q; ax, \Delta\mathbf{R}_{ab} + \hat{x}, i\omega) \right. \end{aligned}$$

$$\begin{aligned}
& - \phi_r(Q; ay, \Delta \mathbf{R}_{ab}, i\omega) - \phi_r(Q; ay, \Delta \mathbf{R}_{ab} + \hat{y}, i\omega) \Big] \\
& \phi_r(Q; aX, \Delta \mathbf{R}_{ab}, i\omega) = \\
& \frac{1}{2\sqrt{2}} \left[ \phi_r(Q; ax, \Delta \mathbf{R}_{ab}, i\omega) - \phi_r(Q; ax, \Delta \mathbf{R}_{ab} + \hat{x}, i\omega) \right] \\
& \phi_r(Q; aY, \Delta \mathbf{R}_{ab}, i\omega) = \\
& \frac{1}{2\sqrt{2}} \left[ -\phi_r(Q; ay, \Delta \mathbf{R}_{ab}, i\omega) + \phi_r(Q; ay, \Delta \mathbf{R}_{ab} + \hat{y}, i\omega) \right].
\end{aligned} \tag{53}$$

Note that this expression for the pair wave function is equivalent to that in Equation (38). The new basis for the  $B$ -particles is simply overcomplete; the  $c$ -numbers  $\bar{c}_{B\sigma'}(\mathbf{R}, i\omega)$  and  $\bar{c}_{B\sigma'}(\mathbf{R}', i\omega)$  for near-neighbor  $\mathbf{R}$  and  $\mathbf{R}'$  are no longer independent.

The new basis is well-adapted for representing pair wave functions for  $\mathbf{Q} = 0$  in a simple way. It is convenient to keep the  $B$ -particle orbital and unit-cell position fixed while varying  $a$  and  $\Delta \mathbf{R}_{ab}$ . For example, separate plots describe the system for the  $B$ -particle in the Cu  $3d_{x^2-y^2}$  orbital ( $\phi_{ad}$ ), in the extended oxygen  $d_{x^2-y^2}$  orbital ( $\phi_{aD}$ ), and in the extended oxygen  $s$  orbital ( $\phi_{aS}$ ). If the pair wave function is to have overall  $d_{x^2-y^2}$  symmetry,  $\phi_{ad}$  and  $\phi_{aD}$  must have *explicit*  $d_{x^2-y^2}$  symmetry in the variable  $\Delta \mathbf{R}_{ab}$ , while  $\phi_{aS}$  must have explicit  $s$  symmetry. (States with  $d$  symmetry may also be constructed for  $b$ -particles in the  $X$  and  $Y$  orbitals. These states are more complicated, since both  $\phi_{aX}$  and  $\phi_{aY}$  must be non-zero.)

In Figure 21 we use histograms to show the spatial variation of the minimum-frequency ( $\omega = \pi T$ ) components of the  $d_{x^2-y^2}$  singlet wave function (i.e., the right eigenvector of the particle-particle kernel) for  $T \sim T_c$ . Recall that this function evolves smoothly into the off-diagonal pair field below  $T_c$ . Each histogram shows a  $4 \times 4$  patch of unit cells, centered on a Cu site in the cell at  $\Delta \mathbf{R}_{ab} = 0$ . The orientation of the  $x$  and  $y$  axes is indicated in Figure 21(a). The height of the block at each point in the lattice is just the value of  $\phi$  at that combination of  $a$ -particle orbital and displacement indices ( $a, \Delta \mathbf{R}_{ab}$ ) for fixed  $B$ -particle indices. It is clear that the wave function is dominated by the  $d$ -orbital components; the  $p$ -orbital components, however, play an important role in determining eigenvalues and transition temperatures, and their neglect is not justified.

Finally the relative frequency dependence of several short-range components of the pair wave function  $\phi_s(\mathbf{0}; ab, \Delta \mathbf{R}_{ab}, i\omega)$  is displayed in Figure 22. Note that, as in the one-band Hubbard model,<sup>21</sup> the wave function is strongly frequency dependent, falling rapidly to zero on a scale of  $\omega \sim 0.5t_{pd}$ .

## E. Eigenvalues and Wave Functions for Particle-Hole Channels

A complete FLEX analysis of the particle-hole (i.e., magnetic and charge density) channels with the same degree of rigor applied in the particle-particle analysis is not attempted here. The reasons are as follows: (i) The version of FLEX considered in the present work and in EB is based on particle-hole exchange. Consequently the particle-particle vertex functions analyzed in the preceding section contain only single-fluctuation-exchange ladders, yet are fully conserving. On the other hand, a fully conserving calculation of the particle-hole vertex functions within this approximation scheme requires the inclusion of not only single-exchange ladders, but also a class of double-exchange Aslamazov-Larkin diagrams.<sup>18,19</sup> Such diagrams constitute the beginning of a parquet-like renormalization of the single-exchange ladders.<sup>14</sup> Since this renormalization is incomplete (and does not improve the consistency of the particle-hole vertices which appear at different points in the calculation), the treatment of the Aslamazov-Larkin diagrams is problematic. (ii) In order to treat the particle-hole vertices on the same footing as the particle-particle, the FLEX approximation should include particle-particle exchange diagrams from the outset (see, e.g., References 14,18,19). Such a treatment, while in principle quite straightforward, exceeds the scope of the present work.

The limitation imposed by these points makes a satisfactory analysis of the nearly singular magnetic channel impossible in the present work. This is because both the double-exchange Aslamazov-Larkin diagrams and the single-exchange diagrams from the crossed particle-particle channel are *repulsive* in the magnetic channel. The omission of these contributions in a naive calculation leads to a drastic overestimate of the magnetic eigenvalue (i.e., values larger than unity). A similar situation has been noted in previous FLEX studies of the one-band Hubbard model;<sup>4,19</sup> in that case the magnetic eigenvalue drops well below unity when the omitted contributions are reinstated.

Note that these limitations in the treatment of the particle-hole channel do not compromise the conserving nature of the FLEX calculation for the particle-particle channel. (This is not to say that satisfying conservation laws guarantees accuracy: the overall lack of self-consistency in two-particle vertices which appear at different points in the FLEX calculation is a broader global concern,<sup>14</sup> which can be remedied only by a more sophisticated parquet-like analysis. See Section V for further comments on this point.)

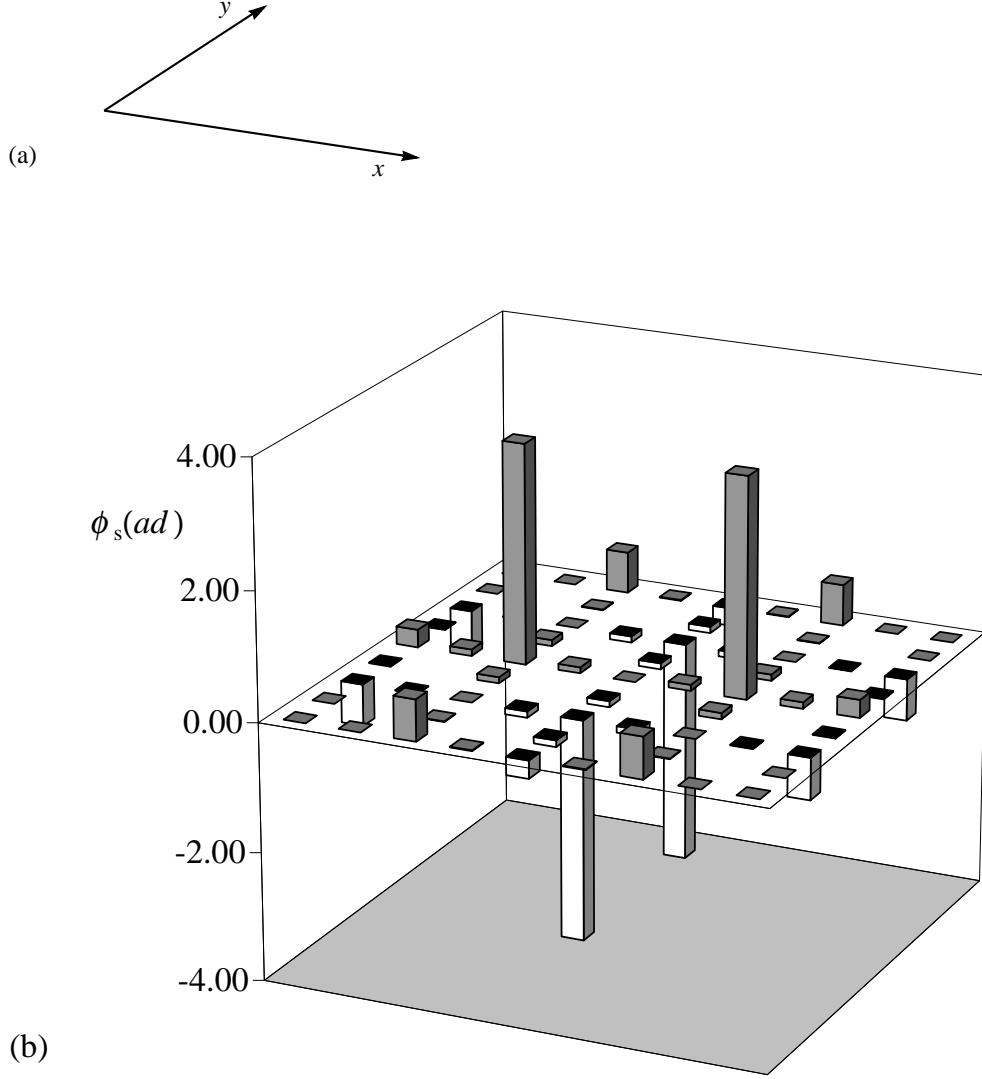


FIG. 21. Relative displacement dependence of the minimum-frequency ( $\omega = \pi T$ ) components of the  $d_{x^2-y^2}$  pair wave function at  $T = t_{pd}/512 = 29$  K for the standard parameter set at  $\langle n \rangle = 1.16$ . The histograms are centered on a Cu site in the cell with  $\Delta \mathbf{R} = 0$ . Note that the wave function is real-valued. (a) Orientation of the  $x$  and  $y$  axes in the histogram plots. (b) Component  $\phi_s(\mathbf{0}; ad, \Delta \mathbf{R}, i\pi T)$ . ( $\Delta \mathbf{R}$  labels the unit-cell displacement to orbital  $a$  from a fixed Cu  $3d_{x^2-y^2}$  orbital.) Note that the histogram exhibits explicit  $d_{x^2-y^2}$  symmetry in this case. (c) Component  $\phi_s(\mathbf{0}; aD, \Delta \mathbf{R}, i\pi T)$ . In this case the fixed orbital is the extended O 2p linear combination with  $d_{x^2-y^2}$  symmetry. As before the histogram exhibits explicit  $d_{x^2-y^2}$  symmetry. Note the difference in scale between this plot and that in (b). (d) Component  $\phi_s(\mathbf{0}; aS, \Delta \mathbf{R}, i\pi T)$ . In this case the fixed orbital is the extended O 2p linear combination with s-wave symmetry. In this case the histogram exhibits explicit s-wave symmetry (see the discussion in the text).

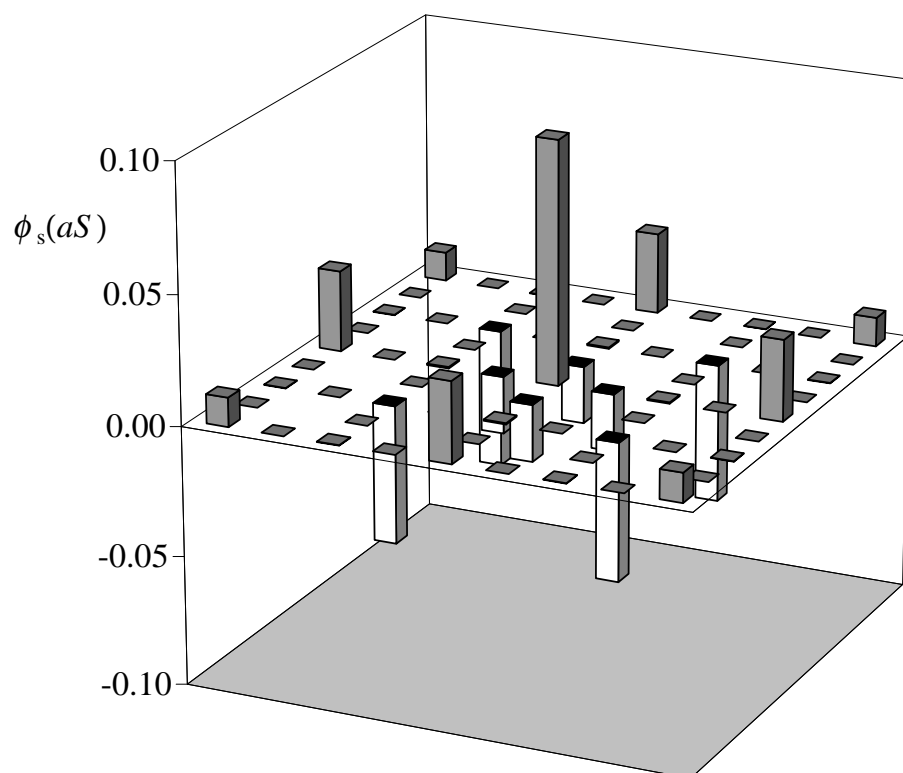
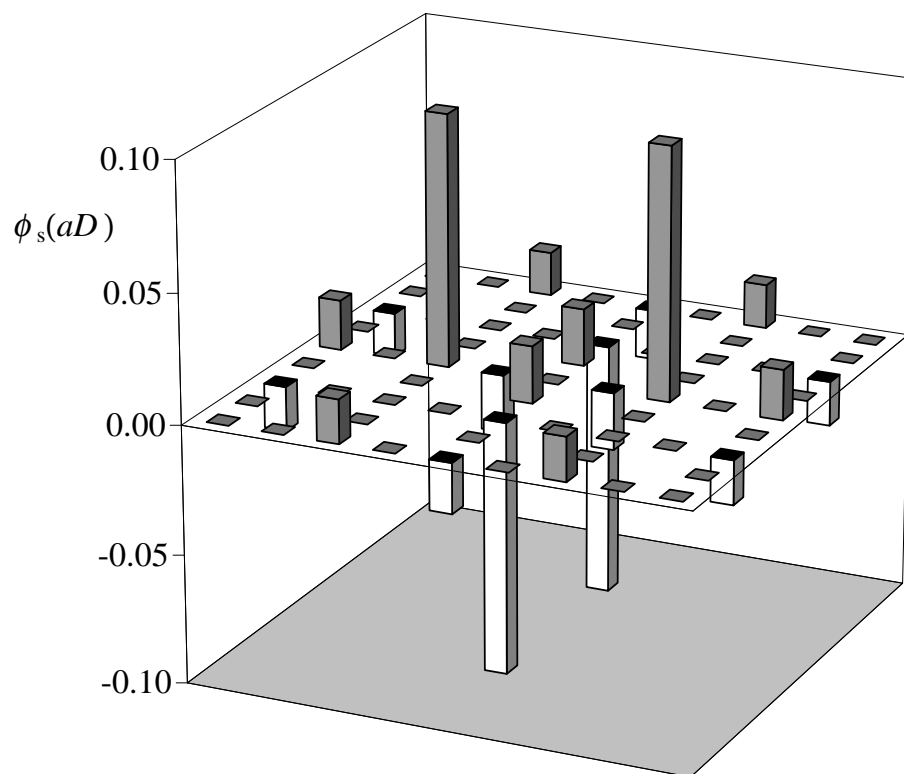


Figure 21 (continued)



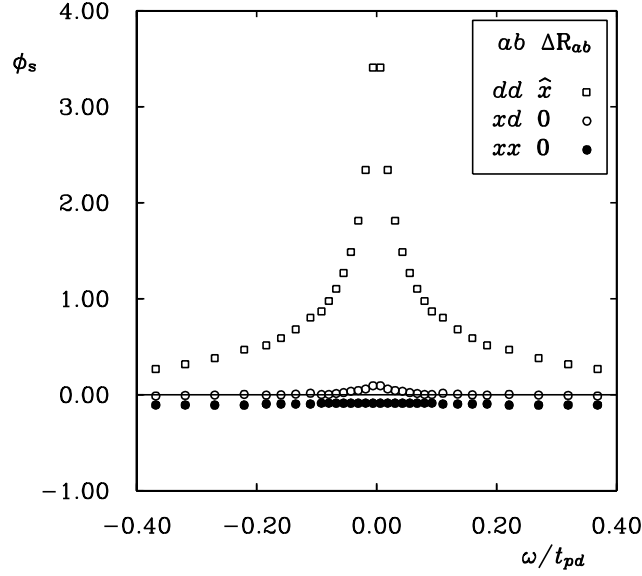


FIG. 22. Relative frequency dependence of short-range components of the  $d_{x^2-y^2}$  pair wave function for the standard parameter set at  $\langle n \rangle = 1.16$ . The dominant component, associated with pairing on near-neighbor Cu  $3d_{x^2-y^2}$  sites, drops to zero over a range determined by the spin fluctuations.

Despite these caveats, we feel it important to emphasize in this section a feature of the physics in the *charge density* channel which has received little attention in recent years.<sup>28</sup> The  $\mathbf{Q} = 0$   $d_{x^2-y^2}$  state in the singlet channel has an analog at  $\mathbf{Q} \sim (\pi, \pi)$  in the density channel. The presence of such an analog or partner state is familiar in a simpler context: in the one-band negative- $U$  Hubbard model,<sup>29,30</sup> the physics near half filling is dominated by a  $\mathbf{Q} = 0$  s-wave singlet state and a  $\mathbf{Q} = (\pi, \pi)$  charge density state. At half-filling these states become exactly degenerate, constituting the components of a Heisenberg-like order parameter. The instability in both the singlet and density channels is driven by the attractive unrenormalized vertex  $-U$ . In the positive- $U$  Hubbard model and the  $\text{CuO}_2$  model, an analogous pair of potential instabilities is driven by the exchange of spin fluctuations. In this case the singlet state of interest has  $d_{x^2-y^2}$  symmetry. The partner state, which becomes exactly degenerate with the  $d_{x^2-y^2}$  singlet at half-filling in the positive- $U$  Hubbard model, is a  $\mathbf{Q} = (\pi, \pi)$  charge density state which shares the discrete  $d_{x^2-y^2}$  rotational symmetry. This state has been previously considered in both weak- and strong-coupling studies.<sup>24,25</sup> We follow Schulz<sup>24</sup> in denoting this state an “orbital antiferromagnet”; the name is natural since the state describes microscopic currents which flow around elementary plaquettes in the square lattice, with the direction of current flow staggered between adjacent plaquettes (see Figure 23). In strong coupling the corresponding state<sup>25,28</sup> has been denoted a “flux phase.”

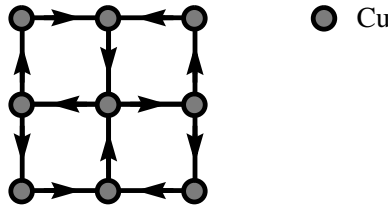


FIG. 23. Representation of the circulating charge density currents in an ordered orbital antiferromagnetic state. The O sites are omitted for clarity.

Away from half-filling in the Hubbard model and at arbitrary fillings in the  $\text{CuO}_2$  model, the exact symmetry between the  $d_{x^2-y^2}$  singlet and the orbital antiferromagnet is broken. Furthermore, with the loss of perfect nesting in the band structure, the wave vector  $\mathbf{Q}$  for the optimal charge density state becomes incommensurate. For example, for the standard parameter set at  $\langle n \rangle = 1.16$  the optimal  $\mathbf{Q}$  vector is approximately  $(1, 0.875)\pi$ .

We have studied the temperature variation of the orbital antiferromagnetic eigenvalue within an inherently limited

approximation: namely, we have included in the charge density vertex only single-exchange diagrams describing magnetic and density fluctuations. As noted above in the comments on the magnetic vertex, this approximation is not entirely satisfactory, since both double-exchange Aslamazov-Larkin diagrams and single-exchange particle-particle ladders are omitted; however, this approximation does preserve the crucial feature which determines both the  $d_{x^2-y^2}$  singlet and orbital antiferromagnetic eigenvalues, i.e., the exchange of nearly antiferromagnetic spin fluctuations.

The temperature variation of the  $d_{x^2-y^2}$  singlet and optimal orbital antiferromagnetic eigenvalues for the standard parameter set is shown in Figure 24. While  $\lambda_{\text{OAF}}$  is smaller than  $\lambda_d$ , the eigenvalues remain very close down to the  $d_{x^2-y^2}$  transition. From this analysis it becomes clear that a fully satisfactory treatment of the model, particularly

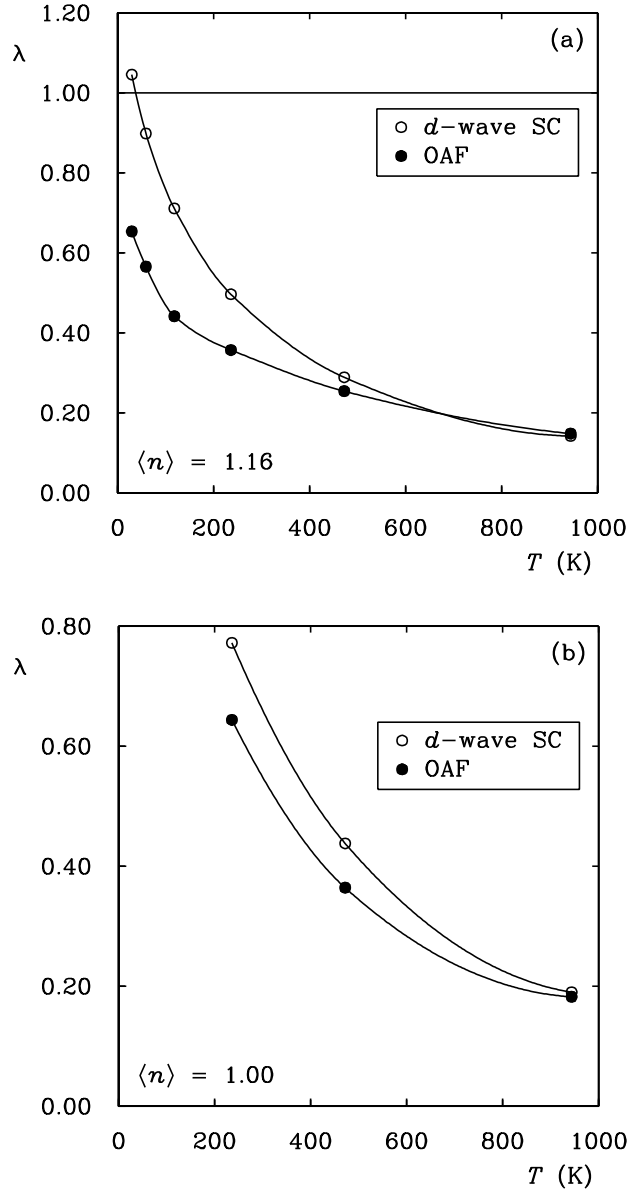


FIG. 24. Temperature dependence of the  $d_{x^2-y^2}$  singlet and orbital antiferromagnetic (OAF) eigenvalues for the standard parameter set. (a) Results for filling  $\langle n \rangle = 1.16$ . The optimal wave vector for the OAF state is in this case  $\mathbf{Q} = (1, 0.875)\pi$ . (b) Results for filling  $\langle n \rangle = 1.00$ . The optimal wave vector is in this case  $\mathbf{Q} = (\pi, \pi)$ .

in the underdoped regime, must describe the competition between the magnetic,  $d_{x^2-y^2}$  singlet, and orbital antiferromagnetic channels. While we have no evidence that the orbital antiferromagnet is ever actually the dominant instability, it is tempting to speculate on its relevance, at least in conjunction with the  $d_{x^2-y^2}$  singlet, for a description of the anisotropic pseudogap observed in many experimental studies.<sup>23</sup>

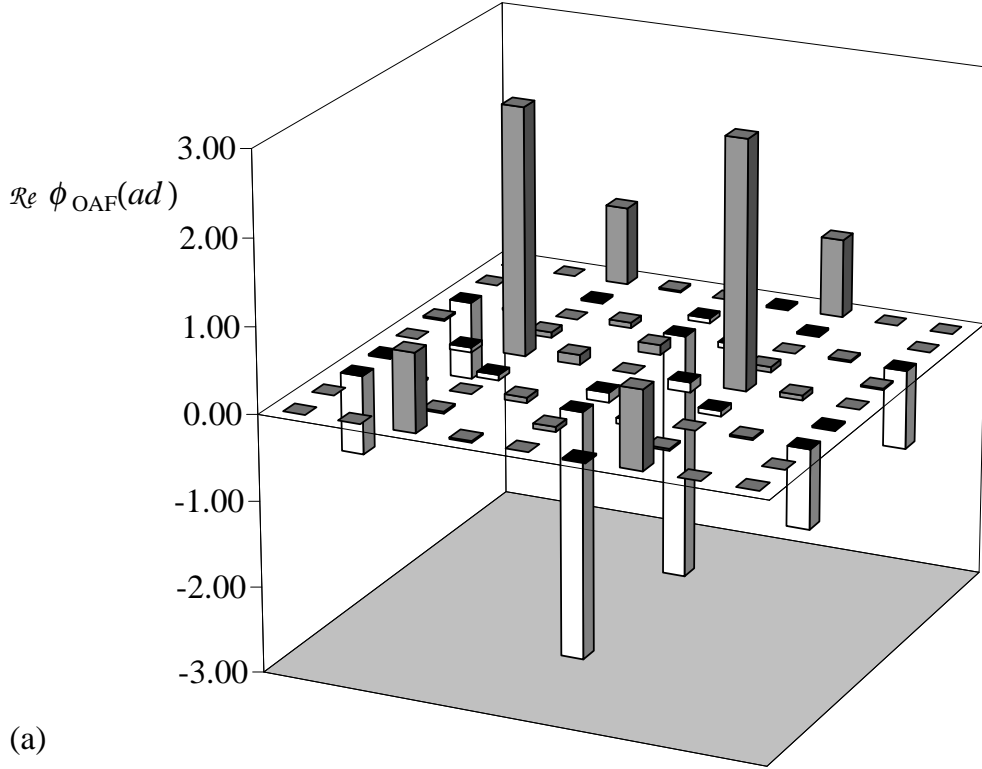


FIG. 25. Relative displacement dependence of the dominant minimum-frequency ( $\omega = \pi T$ ) component of the  $\mathbf{Q} = (\pi, \pi)$  orbital antiferromagnetic wave function,  $\phi_{\text{OAF}}(Q; ad, \Delta\mathbf{R}, i\pi T)$  for the standard parameter set at  $\langle n \rangle = 1.16$ . The temperature is  $T = t_{\text{pd}}/512$ . As in Figure 21, the histograms are centered on a Cu site in the cell with  $\Delta\mathbf{R} = 0$ . In this case the wave function is complex-valued, even though the eigenvalue is real. Note that  $a$  and  $\Delta\mathbf{R}$  vary with  $b = d$  held fixed. Note also the fact that  $d_{x^2-y^2}$  rotational symmetry is manifest for  $a = d$  and arbitrary  $\Delta\mathbf{R}$ , but that the rotational symmetry is hidden for  $a = x$  and  $y$ , as discussed at length in the text. (a) Real part of the wave function. (b) Imaginary part of the wave function.

In Figure 25 we show the spatial variation of the real and imaginary parts of the  $\mathbf{Q} = (\pi, \pi)$  orbital antiferromagnetic wave function  $\phi_{\text{OAF}}(Q; ad, \Delta\mathbf{R}_{ad}, i\omega = i\pi T)$  for the standard parameter set at  $\langle n \rangle = 1.16$  and  $T = t_{\text{pd}}/512$ . The  $d_{x^2-y^2}$  rotational symmetry of the wave function is manifest for the components with  $a = d$ , but is hidden for the components with  $a = x$  and  $y$ . This is true for the following reason: The total wave function takes the form

$$\sum_{\mathbf{R}; ab, \Delta\mathbf{R}_{ab}, \omega} e^{i\mathbf{Q} \cdot (\mathbf{R} + \Delta\mathbf{R}_{ab})} \phi_{\text{OAF}}(Q; ab, \Delta\mathbf{R}_{ab}, i\omega) \times \sum_{\sigma\sigma'} \chi_d^{\sigma\sigma'} \bar{c}_{a\sigma}(\mathbf{R} + \Delta\mathbf{R}_{ab}, i(\omega + \Omega)) c_{b\sigma'}(\mathbf{R}, i\omega), \quad (54)$$

with

$$\chi_d = \frac{1}{\sqrt{2}} \begin{pmatrix} 1 & 0 \\ 0 & 1 \end{pmatrix} \\ \mathbf{Q} = (\pi, \pi) \\ \Omega = 0. \quad (55)$$

It is convenient to adopt the shorthand  $\tilde{a}$  for the rotated image of orbital  $a$  and  $\tilde{\mathbf{R}}_a$  for the rotated image of  $\mathbf{R}_a$ , the unit-cell location of orbital  $a$ . When the wave function coordinates (unit-cell and orbital labels) are rotated, it is guaranteed that the compound d-orbital label  $(a, \mathbf{R}_a) = (d, \mathbf{R})$  maps to  $(\tilde{a}, \tilde{\mathbf{R}}_a) = (d, \tilde{\mathbf{R}})$ , where  $\tilde{\mathbf{R}}$  is the rotated image of  $\mathbf{R}$ . However, under successive rotations, the  $p_x$ -orbital label  $(x, \mathbf{R})$  maps to  $(y, \tilde{\mathbf{R}})$  (rotation through  $\pi/2$ );  $(x, \tilde{\mathbf{R}} - \hat{x})$  (rotation through  $\pi$ ); and  $(y, \tilde{\mathbf{R}} - \hat{y})$  (rotation through  $3\pi/2$ ). A similar set of transformations holds for the  $p_y$ -orbital label. Discrete  $d_{x^2-y^2}$  symmetry requires that

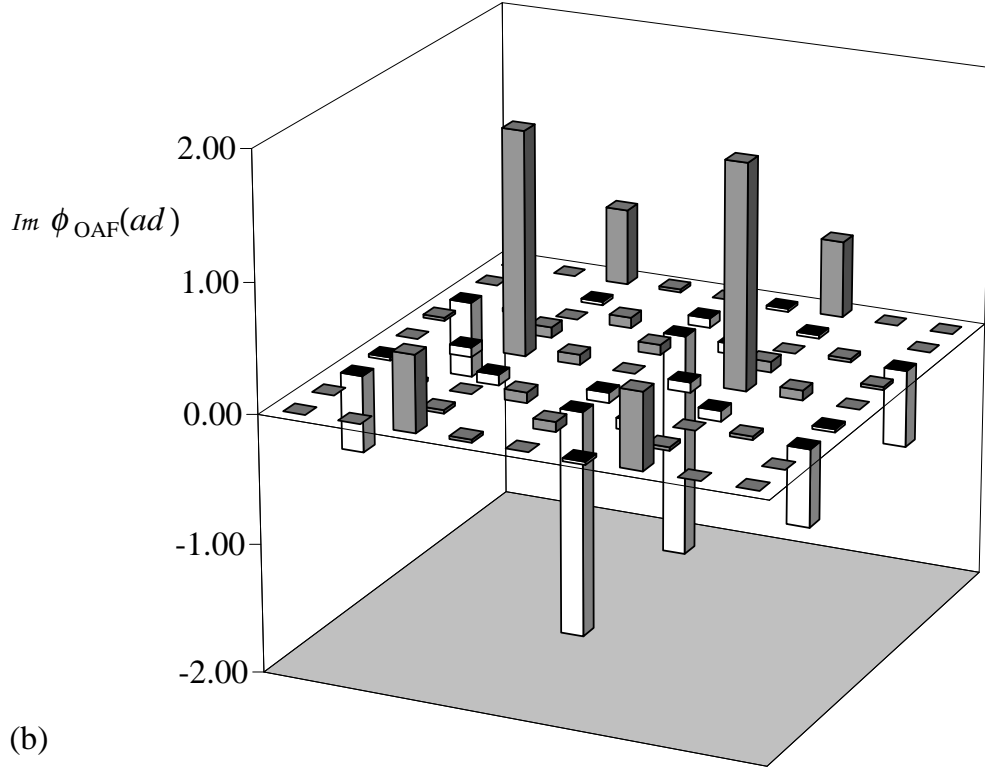


Figure 25 (continued)

$$e^{i\mathbf{Q}\cdot\tilde{\mathbf{R}}_a} \phi_{\text{OAF}}(Q; \tilde{a}\tilde{b}, \tilde{\mathbf{R}}_a - \tilde{\mathbf{R}}_b, i\omega) = e^{2i\theta} e^{i\mathbf{Q}\cdot\mathbf{R}_a} \phi_{\text{OAF}}(Q; ab, \mathbf{R}_a - \mathbf{R}_b, i\omega) , \quad (56)$$

where

$$\begin{aligned} \mathbf{R}_b &= \mathbf{R} \\ \mathbf{R}_a &= \mathbf{R} + \Delta\mathbf{R}_{ab} \\ \theta &= 0, \pi/2, \pi, 3\pi/2 . \end{aligned} \quad (57)$$

When the phase factors  $e^{i\mathbf{Q}\cdot\tilde{\mathbf{R}}_a}$  and  $e^{i\mathbf{Q}\cdot\mathbf{R}_a}$  are equal, the  $d_{x^2-y^2}$  symmetry is manifest in  $\phi_{\text{OAF}}$ , i.e.,

$$\phi_{\text{OAF}}(Q; \tilde{a}\tilde{b}, \tilde{\mathbf{R}}_a - \tilde{\mathbf{R}}_b, i\omega) = e^{2i\theta} \phi_{\text{OAF}}(Q; ab, \mathbf{R}_a - \mathbf{R}_b, i\omega) . \quad (58)$$

However, when

$$e^{i\mathbf{Q}\cdot\tilde{\mathbf{R}}_a} = -e^{i\mathbf{Q}\cdot\mathbf{R}_a} , \quad (59)$$

the  $d_{x^2-y^2}$  symmetry is hidden, i.e.,

$$\phi_{\text{OAF}}(Q; \tilde{a}\tilde{b}, \tilde{\mathbf{R}}_a - \tilde{\mathbf{R}}_b, i\omega) = -e^{2i\theta} \phi_{\text{OAF}}(Q; ab, \mathbf{R}_a - \mathbf{R}_b, i\omega) . \quad (60)$$

This accounts for the seemingly anomalous transformation properties of the  $\phi_{xd}$  and  $\phi_{yd}$  components of the wave function in Figure 25.

The frequency dependence of several short-range components of the  $\mathbf{Q} = (\pi, \pi)$  orbital antiferromagnetic wave function is illustrated in Figure 26. Note that the wave function is in this case intrinsically complex, although the eigenvalue is real. While the Pauli Principle does not dictate the transformation properties under  $\omega \rightarrow -\omega$  in this

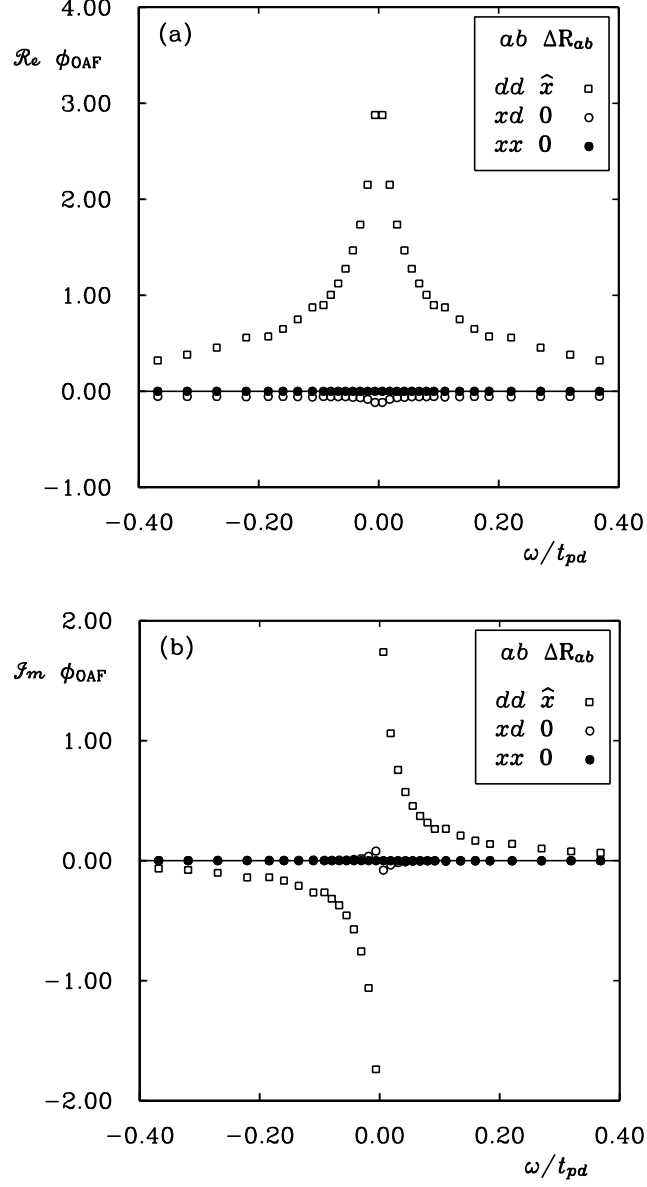


FIG. 26. Relative frequency dependence of short-range components of the  $\mathbf{Q} = (\pi, \pi)$  orbital antiferromagnetic wave function for the standard parameter set at  $\langle n \rangle = 1.16$ . As in Figure 22, the component associated with near-neighbor Cu  $3d_{x^2-y^2}$  sites drops to zero over a range determined by the spin fluctuations. (a) Real part of the wave function. (b) Imaginary part of the wave function.

case, the overall phase of the wave function for  $\mathbf{Q} = (\pi, \pi)$  and  $\Omega = 0$  may still be chosen such that

$$\phi_{\text{OAF}}(Q; ab, \Delta\mathbf{R}, -i\omega)^* = \phi_{\text{OAF}}(Q; ab, \Delta\mathbf{R}, i\omega) . \quad (61)$$

This follows from a basic symmetry of the eigenvalue problem for  $K_{\Gamma}^{\text{ph}} \equiv \Gamma_{\Gamma}^{\text{ph}} G^{\text{ph}}$  in Equation (32), viz.,

$$\begin{aligned} K_{\Gamma}^{\text{ph}}(Q; m_1 m_2, \Delta\mathbf{R}_{12}, i\omega; m_3 m_4, \Delta\mathbf{R}_{34}, i\omega')^* = \\ K_{\Gamma}^{\text{ph}}(-Q; m_1 m_2, \Delta\mathbf{R}_{12}, -i\omega; m_3 m_4, \Delta\mathbf{R}_{34}, -i\omega') . \end{aligned} \quad (62)$$

This implies that if  $\phi(Q; ab, \Delta\mathbf{R}, i\omega)$  is an eigenfunction with eigenvalue  $\lambda(Q)$  for total momentum-frequency  $Q$ , then  $\phi(Q; ab, \Delta\mathbf{R}, -i\omega)^*$  is an eigenfunction with eigenvalue  $\lambda(Q)^*$  for total momentum-frequency  $-Q$ . For the case of interest here  $Q = -Q$ , the eigenfunction  $\phi(Q; ab, \Delta\mathbf{R}, i\omega)$  is non-degenerate, and the eigenvalue is real. Thus,

$$\phi(Q; ab, \Delta\mathbf{R}, -i\omega)^* = \alpha \phi(Q; ab, \Delta\mathbf{R}, i\omega) , \quad (63)$$

with  $\alpha$  a complex constant. The constant may always be set equal to unity by a simple rescaling of  $\phi$ , leading to the symmetry relation in Equation (61). Symmetries for general  $\mathbf{Q}$  near  $(\pi, \pi)$  may be examined by an extension of this argument. Note finally the overall similarity of the  $d_{x^2-y^2}$  singlet wave function plotted in Figures 21–22 and the orbital antiferromagnetic wave function plotted in Figures 25–26, with respect to both spatial and frequency dependence.

## V. SUMMARY

Our results demonstrate that the fluctuation exchange approximation provides reasonable results for both the magnitude and doping dependence of the  $d_{x^2-y^2}$  transition temperature in the overdoped regime,  $\langle n \rangle - 1 > 0.16$ . While the level of quantitative agreement between FLEX and experiment<sup>26</sup> is almost certainly fortuitous, it is important to emphasize several points in this regard: (i) For a wide range of model parameters clustered around the standard LDA set,<sup>9</sup> FLEX transition temperatures are predicted in the range of 10 to 100 K. It is by no means obvious that this should be so, i.e., one might have imagined obtaining a range of transitions stretching over several orders of magnitude. (ii) The continued rise of the FLEX  $d_{x^2-y^2}$  eigenvalue for values of  $\langle n \rangle$  approaching unity is consistent with previous Monte Carlo studies,<sup>19</sup> which have demonstrated enhanced  $d_{x^2-y^2}$  correlations even in regions where long-range magnetic order is being established. It appears clear that a more sophisticated approach<sup>14</sup> is essential to resolve the competition between the incipient instabilities in the antiferromagnetic spin,  $d_{x^2-y^2}$  singlet, and orbital antiferromagnetic channels in the underdoped regime  $\langle n \rangle \rightarrow 1.0$ .

As emphasized in Section IV, the presence of large eigenvalues in the orbital antiferromagnetic channel is an unambiguous result of our analysis, despite the technical limitations of our approach for the particle-hole channels. It is important to note that the orbital antiferromagnetic channel becomes degenerate with the  $d_{x^2-y^2}$  singlet to form a Heisenberg-like order parameter in models with exact particle-hole symmetry (such as the half-filled one-band Hubbard model). While the breaking of particle-hole symmetry in the standard  $\text{CuO}_2$  model apparently favors the  $d_{x^2-y^2}$  singlet at half-filling, it seems clear that the orbital antiferromagnet must be retained in any analysis which aims at a quantitative description of the region near  $\langle n \rangle = 1$ .

Finally, as a more general comment, the present study demonstrates the feasibility of extending the FLEX instability analysis to models with an increasing degree of realism. While the principal shortcoming of FLEX, viz., the lack of self-consistency at the two-body level, remains a separate concern, it is also clear that progress toward a truly predictive many-body theory demands the ability to incorporate realistic details of lattice and interaction structure. A natural next step in this direction is the analysis of a one-band model with longer-range interactions. The general formalism developed in the present work and in EB (in particular, the use of a real-space basis set for relative coordinates) provides a computationally feasible framework for such a study.

## ACKNOWLEDGMENTS

This work was supported in part by the National Science Foundation under grants DMR95–20636 and PHY94–07194; and by the Department of Energy under grant 85–ER–45197. NEB gratefully acknowledges the hospitality of the Institute for Theoretical Physics where this work was begun. We also thank D. J. Scalapino, N. Bulut, and C.-H. Pao for a series of fruitful discussions.

- <sup>1</sup> See, e.g., the extensive review by D. J. Scalapino, *Physics Reports* **250**, 329 (1995).
- <sup>2</sup> D. J. Scalapino, E. Loh, and J. E. Hirsch, *Phys. Rev. B* **34**, 8190 (1986); K. Miyake, S. Schmitt-Rink, and C. M. Varma, *Phys. Rev. B* **34**, 6554 (1986).
- <sup>3</sup> N. E. Bickers, D. J. Scalapino, and R. T. Scalettar, *Int. J. Mod. Phys. B* **1**, 687 (1987).
- <sup>4</sup> N. E. Bickers, D. J. Scalapino, and S. R. White, *Phys. Rev. Lett.* **62**, 961 (1989).
- <sup>5</sup> A. E. Ruckenstein, P. J. Hirschfeld, and J. Appel, *Phys. Rev. B* **36**, 857 (1987); G. Kotliar, *Phys. Rev. B* **37**, 3664 (1988).
- <sup>6</sup> See also the phenomenological studies by P. Monthoux, A. V. Balatsky, and D. Pines, *Phys. Rev. Lett.* **67**, 3448 (1991); P. Monthoux and D. Pines, *ibid.* **69**, 961 (1992); S. Lenck, J. P. Carbotte, and R. C. Dynes, *Phys. Rev. B* **49**, 4176 (1994).
- <sup>7</sup> V. J. Emery, *Phys. Rev. Lett.* **58**, 2794 (1987).
- <sup>8</sup> F. C. Zhang and T. M. Rice, *Phys. Rev. B* **37**, 3759 (1988).
- <sup>9</sup> M. S. Hybertsen, M. Schlüter, and N. E. Christensen, *Phys. Rev. B* **39**, 9028 (1989).
- <sup>10</sup> A. K. McMahan, R. M. Martin, and S. Satpathy, *Phys. Rev. B* **38**, 6650 (1988).
- <sup>11</sup> E. B. Stechel and D. R. Jennison, *Phys. Rev. B* **38**, 4632 (1988).
- <sup>12</sup> Gökhan Esirgen and N. E. Bickers, *Phys. Rev. B* **55**, 2122 (1997).
- <sup>13</sup> An earlier normal-state study of the CuO<sub>2</sub> model with  $U_{pp} = U_{pd} = 0$  was carried out by J. Luo and N. E. Bickers, *Phys. Rev. B* **47**, 12153 (1993).
- <sup>14</sup> N. E. Bickers, in *Numerical Methods for Lattice Quantum Many-Body Problems* (Addison Wesley, Reading MA, in press).
- <sup>15</sup> Such a basis set was first employed in the context of the CuO<sub>2</sub> model by P. B. Littlewood, C. M. Varma, S. Schmitt-Rink, and E. Abrahams, *Phys. Rev. B* **39**, 12371 (1989). See also Y. Bang, K. Quader, E. Abrahams, and P. B. Littlewood, *Phys. Rev. B* **42**, 4865 (1990).
- <sup>16</sup> D. C. Sorensen, *SIAM J. Matr. Anal. Apps.* **13**, 357 (1992); B. N. Parlett and Y. Saad, *Linear Algebra and its Applications* **88/89**, 575 (1987). A publicly available version of the Lanczos-Arnoldi algorithm resides in the ARPACK Internet library.
- <sup>17</sup> G. Baym and L. P. Kadanoff, *Phys. Rev.* **124**, 287 (1961); G. Baym, *ibid.* **127**, 1391 (1962). See also the discussion in Reference 14.
- <sup>18</sup> N. E. Bickers and D. J. Scalapino, *Ann. Phys. (N. Y.)* **193**, 206 (1989).
- <sup>19</sup> N. E. Bickers and S. R. White, *Phys. Rev. B* **43**, 8044 (1991).
- <sup>20</sup> Chien-Hua Pao and N. E. Bickers, *Phys. Rev. B* **49**, 1586 (1994).
- <sup>21</sup> Chien-Hua Pao and N. E. Bickers, *Phys. Rev. Lett.* **72**, 1870 (1994); *Phys. Rev. B* **51**, 16310 (1995).
- <sup>22</sup> See, e.g., C. Itzykson and J.-M. Drouffe, *Statistical Field Theory*, (Cambridge University Press, 1989), Vol. 1.
- <sup>23</sup> See, e.g., the following and references therein: Z.-X. Shen and J. R. Schrieffer, *Phys. Rev. Lett.* **78**, 1771 (1997) (ARPES); R. Nemetschek *et al.*, *Phys. Rev. Lett.* **78**, 4837 (1997) (Raman); and G. V. M. Williams *et al.*, *Phys. Rev. Lett.* **78**, 721 (1997) (NMR).
- <sup>24</sup> H. J. Schulz, *Phys. Rev. B* **39**, 2940 (1989).
- <sup>25</sup> I. Affleck and J. B. Marston, *Phys. Rev. B* **37**, 3774 (1988).
- <sup>26</sup> M. K. Crawford *et al.*, *Phys. Rev. B* **41**, 282 (1990).
- <sup>27</sup> See, e.g., D. J. Scalapino, in *Superconductivity*, edited by R. D. Parks (Marcel Dekker, New York, 1969), Vol. 1.
- <sup>28</sup> Note, however, the recent re-analysis of the flux phase by X.-G. Wen and P. A. Lee, *Phys. Rev. Lett.* **76**, 503 (1996).
- <sup>29</sup> See, e.g., A. Moreo and D. J. Scalapino, *Phys. Rev. Lett.* **66**, 946 (1991), and references therein.
- <sup>30</sup> J. Luo and N. E. Bickers, *Phys. Rev. B* **48**, 15983 (1993).